RICE UNIVERSITY

Photoresponse of bowtie nanojunctions

by

Kenneth Mellinger Evans

A Thesis Submitted
in Partial Fulfillment of the
Requirements for the Degree

Doctor of Philosophy

Approved, Thesis Committee:

Douglas Natelson, Chair
Professor of Physics and Astronomy

Peter Nordlander
Professor of Physics and Astronomy

Michael S. Wong
Professor in Chemical and Biomolecular Engineering

Houston, Texas

July, 2015

Abstract

Photoresponse of bowtie nanojunctions

by

Kenneth Mellinger Evans

Plasmon resonant nanostructures provide a platform for controlling light on sub-wavelength lengthscales. Integrating plasmonic materials into dielectric environments, as well as its compliment – addressing nanoscale photonic elements with plasmon active geometries – is a challenging aspect of current research in wide variety of scientific disciplines including microscopy, photovoltaics, photonics, and catalytic chemistry. This thesis covers two experiments with the goal of electrically and optically addressing nanoscale volumes of semiconducting material using Au nanojunctions with plasmon resonant electrodes.

The first measurement aims to use the large field enhancements in bowtie nanojunctions to trap semiconducting nanocrystals from solution. Trapped nanocrystals could then potentially span the gap between the structure's two electrodes to serve as an active optical and electrical region for a number of desirable photoresponsive measurements in single to few nanocrystal systems. We establish a numerical model simulating the force applied on nanocrystals in and around the nanogap as result of

the structure's plasmon modes. We also provide experimental data of trapping events in bowtie nanogaps and measurements of the photocurrent generated in the resultant Au-nanocrystal devices. The challenges of this project, mostly related to ligand and surface chemistry, are discussed.

In the second experiment, we demonstrate plasmon-enhanced photoconduction in Au bowtie nanojunctions containing nanogaps overlaid with an amorphous Ge film. The role of plasmons in the production of nanogap photocurrent is verified by studying the unusual polarization dependence of the photoresponse. With increasing Ge thickness, the nanogap polarization of the photoresponse rotates 90°, indicating a change in the dominant relevant plasmon mode, from the resonant transverse plasmon at low thicknesses to the nonresonant "lightning rod" mode at higher thicknesses. To understand the plasmon response in the presence of the Ge overlayer and whether the Ge degrades the Au plasmonic properties, we investigate the photothermal response (from the temperature-dependent Au resistivity) in no-gap nanowire structures, as a function of Ge film thickness and nanowire geometry. The film thickness and geometry dependence are modeled using a cross-sectional, finite element simulation. The no-gap structures and the modeling confirm that the striking change in nanogap polarization response results from redshifting of the resonant transverse mode, rather than degradation in the Au/Ge properties. We note remaining challenges in determining the precise mechanism of photocurrent production in the nanogap structures.

Acknowledgments

I would first like to thank my thesis advisor, Dr. Douglas Natelson, who made my research experience at Rice possible. Throughout my tenure in his lab, Doug has been patient, optimistic, and generous with his time. Listening to Doug give short physics lessons at group meetings and during visits down to the lab has been a consistent highlight from my time in the department.

I want to express my gratitude to my two other committee members, Dr. Peter Nordlander and Dr. Michael Wong, for taking the time to read and review this manuscript and participate in my defense.

I would next like to thank Dr. Kirstin Matthews. For the past five years, Kirstin has been a wonderful resource on just about every aspect of my life. She continues to give me opportunities to learn and work, and I am grateful to have her in my corner as I figure out what I want to do next.

I want thank everyone who has come through the Natelson lab over the past seven years. I've had a chance to learn something from pretty much every person that has spent even a few weeks in the lab. I especially want to thank Pavlo for dedicating so much time toward the completion of my project. I also want to say thanks to Will, Jenny, and Joey for lending a helpful ear whenever I need to air out an idea or problem. Also I'd like to thank Heng, Ruoyo, Charlotte, and Ben for brightening the lab.

My life outside Rice has been so full of friends and positive content the last four

years that I'd like to thank the entire city of Houston for having so many fun and based individuals living in it. I want to thank Chanelle and Matthew and Taylor and Austin and Jessica and Marina and Heather and Anna and Amanda for their friendship and support over the years.

I want to express my gratitude to Jordan, my basketball coach for the last five years. He rules and so did every game I played with the men's club team.

I want to say thank you to Saray and Sarah for taking jobs in the physics department this year. Y'all also rule.

Finally, I want to thank my family for their love and support through every part of my education: my dad, my brother, Russell, and my sister, Jill, my family in Pennsylvania, and my family on the west coast. Y'all are the best. Finally, I'd like to dedicate this thesis to my grandmother, Arlene Carvell.

Contents

Illustrations

Chapter 1

Introduction

1.1 Preface

This thesis will cover two experiments studying the photoresponse of devices made using Au bowtie nanojunctions. These structures have been shown to be ideal geometries for assessing the electronic and optical properties of single molecules, and other materials, as well as understanding more fundamental processes in nanoscale devices such as heat dissipation, photocarrier generation, and plasmon response. Chapter 1 will provide a background to introduce topics covered in the later chapters. Chapter 2 describes experimental efforts and provides a theoretical model for plasmonic optical trapping in bowtie nanogaps as a potential method for creating nanocrystal based optoelectronic devices. Chapter 3 will discuss recent experiments measuring photocurrent and optically induced heating in plasmon resonant nanojunctions overlayed with an amorphous Ge film. Additionally, it reviews several other relevant experiments demonstrating field enhanced photoconduction in plasmonic nanoantennas.

1.2 Experimental Significance

Plasmonic nanostructures have proven to be a useful tool for concentrating light on subwavelength spatial scales. Embedding plasmon resonant antennas into light

sensitive devices has the potential to increase device responsivity through both electromagnetic field enhancement and other plasmon-based mechanisms that can generate additional photocarriers. Understanding the impact of of various plasmon modes and the relative contribution to the total photoresponse of different carrier production processes remains challenging. This thesis addresses these challenges with experimental data, numerical models, and a discussion on recent advances in plasmon-assisted optoelectronics.

The plasmon-enhanced photosensitive devices in this work are created by overlaying an amorphous Ge film on Au nanojunctions. The plasmon modes of the resultant structures are investigated through photocurrent measurements of bowtie nanojunctions as well as optically induced heating in "unbroken" nanowires. This system provides a platform for understanding changes in the plasmon response of metal nanostructures in the presence of dielectrics and demonstrates the ability to use semiconducting material to tune plasmon resonances. This knowledge will important for integrating plasmon-active materials into traditional photosensitive systems.

This work marks one of the first studies demonstrating plasmon assisted photocurrent in individual nanoantennas. Further, the devices have a truly nanoscale active optical region. The novelty and scale of this work make it an important step forward toward integrating subwavelength plasmonic elements into existing photodetection platforms.

1.3 Background

1.3.1 Plasmons

Plasmons are collective oscillations of free electrons moving against a stationary lattice of positive ions in a metal. Resonant excitation of plasmons in metal nanostructures produce local fluctuations to the electron density. These changes in charge density can result in large enhancements to the electric field near the surface of the metal.

Plasmonic nanostructures are known to have large absorption cross sections that can extend far beyond their geometric size. In the simplest case, a spherical nanoparticle in the Rayleigh approximation, where the particle's diameter is much smaller than the wavelength of incident radiation (i.e. in Equation 1.2 when $x \ll 1$), has a normalized absorption cross section, or "efficiency factor", given by[5]:

$$Q_{abs} \backsimeq 4xIm\left(\frac{\epsilon - 1}{\epsilon + 2}\right) \tag{1.1}$$

where

$$x = \frac{C}{2\pi a/\lambda} \tag{1.2}$$

where C is the circumference of the particle, a is its radius, and $\epsilon = \epsilon_1 + i\epsilon_2$ is the frequency dependent dielectric function of the material. The dielectric function describes the material's response to an applied electric field; ϵ_1 is a measure of the how much the material becomes polarized in response to this field, i.e. energy "stored", and ϵ_2 describes the destructive interference due to a phase delay between the material

response and the field itself, i.e. energy "loss".

At low energies, the dielectric constant for Au can be well described by the Drude model for free electrons, given by[6]:

$$\epsilon(\omega) = \epsilon_\infty - \frac{\omega_p^2}{\omega^2 + i\gamma\omega} \tag{1.3}$$

where ϵ_∞ is the dielectric constant in the high frequency limit, ω_p is the bulk plasma frequency, and γ is a damping constant. It is clear from Equation 1.1 that when $\epsilon_1 \to -2$ and if $\epsilon_2 \ll 1$ the absorption cross section will become large. There are many materials that meet these criteria at convenient wavelengths, such as copper, silver, and gold. Experimental values for these materials in bulk can be found in Johnson and Christy (1972)[7]. While these resonance conditions will also vary on the geometry of the system, for bare Au nanojunctions described in this thesis they have been experimentally and theoretically found to be satisfied in the near-IR[8].

The resultant field enhancements and large absorption cross sections of plasmonic nanostructures have been used in a wide variety of applications including surface-enhanced Raman spectroscopy (SERS)[9, 10], subwavelength optics[11, 12], plasmonic optical trapping[13, 14, 15, 16], and plasmon-assisted photodetection and photovoltaics[17, 18, 19, 20, 21, 22].

1.3.2 Plasmons in nanojunctions

Nanojunctions refer to a class of metal nanostructures consisting of two electrodes separated by a small gap, typically on the order of several nanometers. There are a variety of experimental techniques for achieving gaps of this size, most notably mechanical break junctions[23], scanning tunneling microscope style probes[24], and lithographically defined nanowires. The first two often rely on ensemble averages to look at quantum effects in atomic-scale devices. Lithographic nanojunctions patterned onto substrates allow for stable, long-term device performance, even at room temperature, and have been shown to act as combined optical antennas and electrical probes[25].

Gaps in lithographic nanowires are created by one of two methods: by electromigration[26] or through the "self-aligned" fabrication process[27]. In the case of electromigration, only a single lithography step is needed to define a nanowire constriction between two larger electrodes. The wires are typically 100-130 nm in width and 13-15 nm in thickness. The wires are "broken" through a series of well-controlled current pulses, automated in LabView. The pulses push apart gold atoms breaking the constriction into two sides (Figure 1.1). Breaking occurs through a combination of two processes: by the electronic wind force, in which conduction electrons transfer momentum to the gold atoms at a high enough bias, and from the electric field pushing charge defects in the wire.

Conduction through both electromigrated and self-aligned bowtie nanogaps has

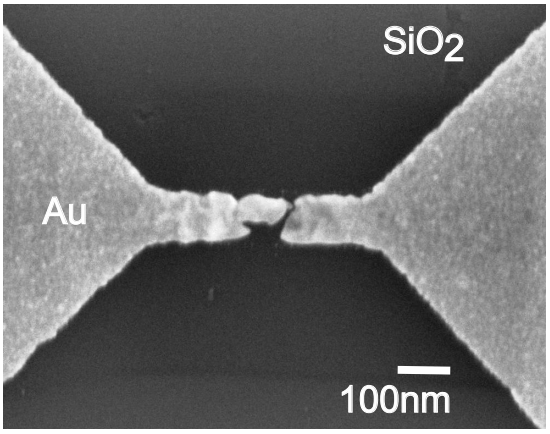

Figure 1.1 : A scanning electron microscope (SEM) image of a typical bare, electromigrated bowtie nanogap with width 120 +/- 5 nm.

been shown to be dominated by roughly a molecular volume[28]. Both structures provide a certain degree of control – breaking procedure in the former, fabrication parameters in the latter – in creating a variety of gap sizes which can create a range of stable conductance values. In most cases, bare electromigrated devices at room temperature are characteristic of traditional tunnel junctions; current as a function of voltage is weakly non-linear, approximately symmetric at zero bias, and passing through zero current at zero bias. However, electromigrated junctions will typically become more resistive with time as the gap widens with continued electric and optical measurements. Alternatively, self-aligned devices can maintain more stable conductance configurations, but they require an extra time-intensive lithographic step (Figure 3.1b). Fabrication procedures for self-aligned nanojunctions are described in detail in Section 1.4.

Previous work in the Natelson lab, conducted primarily by Dr. Daniel Ward, Dr.

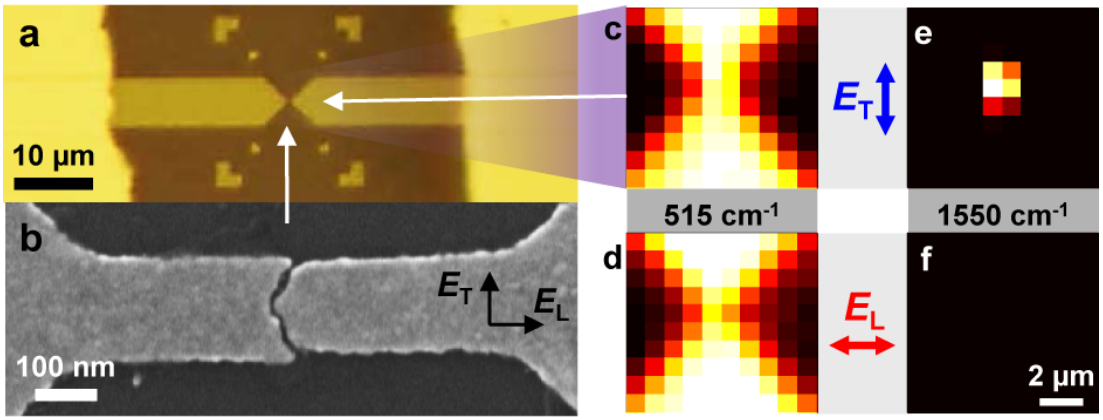

Figure 1.2 : (a) An optical micrograph of a typical device. (b) A SEM image of a self-aligned nanojunction. (c,d) A spatial map of the silicon Raman line (510-520 cm^{-1}) for transverse and longitudinal polarizations, respectively. (e,f) A spatial map of the an integrated spectrum for BPE (1500-1600 cm^{-1}) for transverse and longitudinal polarizations, respectively. Figure taken from Herzog, *et al.* (2013)[1].

Joesph Herzog, and Yajing Li, has studied the SERS response of molecules, such as P3HT, *p*MA, and C60, in bowtie nanogaps[8, 9, 10, 29]. Creating spatial maps of the Raman response in Au nanojunctions reveals "hotspots" localized to the gap center for Raman lines specific to the molecule (Figure 1.2e). Changes in the Raman spectra have been shown to be correlated fluctuations in the electronic conduction. Similar experiments demonstrating SERS in nanoantennas have been reported in many other optical antenna-based configurations[30, 31, 32].

The plasmon response in bowtie nanojunctions has been shown to be dominated by a transverse resonant mode, maximized when the incident laser illumination is polarized perpendicular to the length of the constriction ($\theta = 90°$). An example

can be seen in Figure 1.2 measuring the SERS signal from *trans*-1,2-bis(4-pyridyl)-ethylene (BPE) in self-aligned nanojunctions; the hotspot for the Raman spectrum of the molecule is undetectably weak at longitudinal polarization[1]. This polarization dependence is in contrast to expectations of the "lightning rod" effect, when the maximum plasmon response occurs when the incident polarization is parallel to the elongated direction of a metal wire or tip, from the excitation of longitudinal or tip plasmons[33]. This polarization response occurs due to the transverse plasmon mode of the nanojunction coupling to hybridized "dark", or non-radiative, modes at the gap edges. This hypothesis has been verified with both extensive COMSOL modeling and cathodoluminescence measurements[34].

1.3.3 Photocarrier generation in metal-semiconductor-metal junctions

Individual nanoscale light emitting and absorbing devices are desirable photonic elements but remain difficult to fabricate in bulk. Nanojunctions provide a potential structural platform for integrating semiconducting materials, such as quantum dots (discussed in Section 1.3.5), into nanoscale circuits as active optical elements[35, 36, 37, 38, 39].

Utilizing plasmon resonant materials as electrodes in these devices has the potential to increase their efficiency by a variety of plasmon-coupled photocarrier generation mechanisms[20, 40, 41, 42, 43, 44]. In metal-semiconductor-metal nanojunctions these processes include: direct absorption of light in the semiconductor located at the gap,

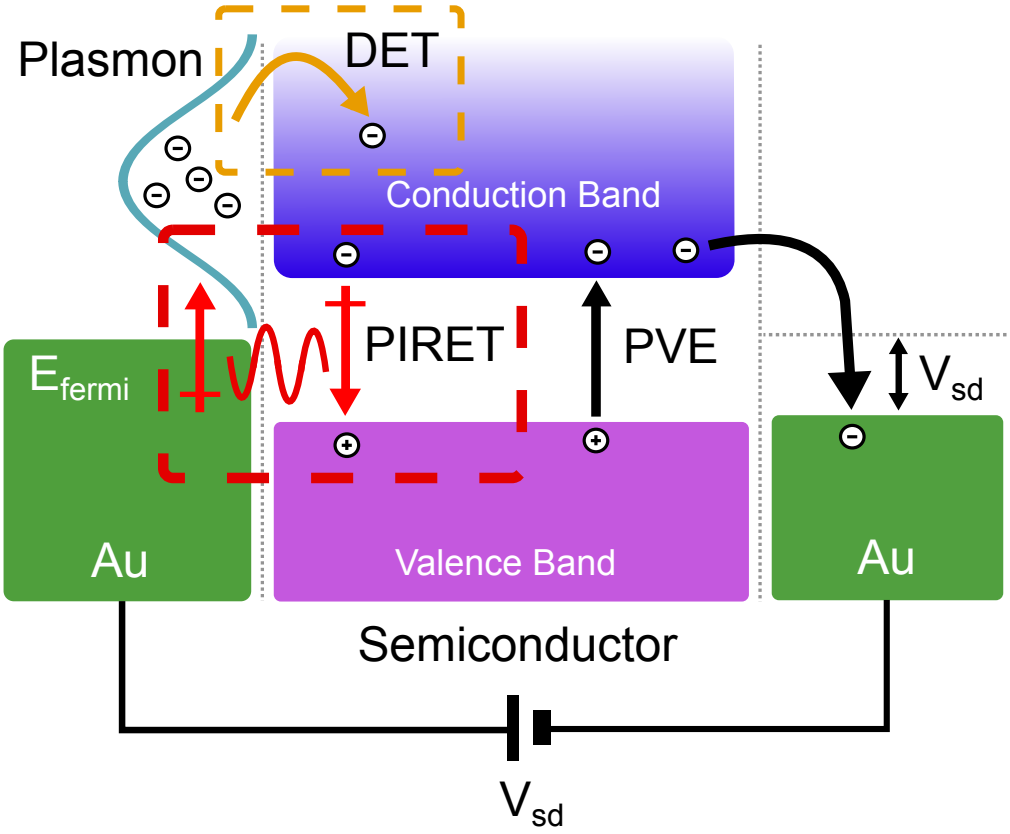

Figure 1.3 : A schematic of various relevant carrier production processes in plasmon resonant, metal-semiconductor-metal devices. Photogenerated electrons can be excited across the semiconductor bandgap via PVE or directly injected from the plasmon resonant metal electrodes via DET and PIRET. Figure adapted from Cushing, *et al.* (2012)[2].

creating electron-hole pairs via the photovoltaic effect (PVE); driving high-energy, or "hot", carriers generated in the plasmon across the semiconductor-metal barrier, also known as direct electron transfer (DET); or through plasmon-induced resonant energy transfer (PIRET), where the plasmon can directly excite electron-hole pairs in the semiconductor (Figure 1.3) [2, 45]. Optical rectification[42, 46] and the photothermoelectric effect (PTE)[47, 48] have also been reported to produce photocurrent in similar structures. PTE is the optically driven version of the Seebeck effect, where incident radiation locally heats a material, inducing a temperature gradient across it, and in turn produces a voltage. The ratio of the voltage generated to the temperature difference created is known and the Seebeck coefficient, which is specific to the material. At an interface between two materials with different Seebeck coefficients, a net voltage will be generated across the interface[49].

Hot electron-hole pairs can be generated in metal nanostructures when plasmons decay non-radiatively through a process known as Landau damping[50]. While previously considered as a type of loss in optical devices, it has since been shown that hot electrons can be "caught" by placing a semiconductor or oxide in contact with the plasmon resonant structure, creating a Schottky barrier. Their injection as photocurrent then depends only the height of this barrier and not the size of the semiconductor bandgap. In this way absorption over a wider range of incident photon energies is possible. However, hot carriers have short lifetimes, typically on the order of 100 fs to 1 ps. Efficient injection over the barrier requires a careful consideration of geometry

and materials as well as the bandstructure of the neighboring semiconductor to ensure carriers do not recombine or otherwise thermalize before crossing[51]. Individual photovoltaic devices operating solely on plasmon-coupled mechanisms remain challenging to fabricate and have comparatively low responsivities to traditional PVE photodetectors. Nevertheless, hot carrier generation in plasmonic nanoantennas has been observed in many independent studies over the last five years[17, 43, 52, 53, 54, 55, 56].

The most recent effort, by Hong, *et al.* (2015)[43], is a major step toward understanding photocurrent in plasmon-assisted optoelectronic devices. By sweeping the energy of the incident radiation, the authors demonstrate a transition from traditional PVE produced photocurrent when the excitation wavelength is above the bandgap energy that of the active material (MoS_2), to a combined hot electron and PTE produced photocurrent when the the excitation wavelength is below the bandgap. This transition is verified through studying the polarization dependence of the photocurrent, which shifts from being maximized for longitudinal excitation above bandgap to being dominated the transverse excitation mode below bandgap. Shi, *et al.* (2011)[42], and Tang, *et al.* (2008)[41] have performed similar polarization studies, using two different materials with plasmon active electrodes (graphene and crystalline Ge, respectively). However, understanding the relative contributions of plasmon-coupled photocarrier production versus PVE or other mechanisms has yet to be explored extensively in the literature.

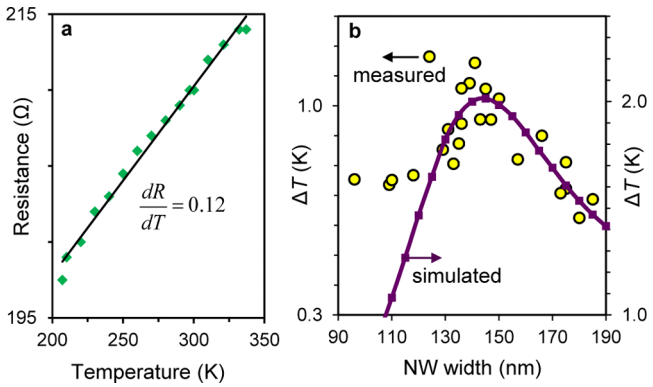

Figure 1.4 : (a) Experimental data measuring the change in resistance in no-gap bowties (130 nm wide, 1 nm / 13 nm thick Ti / Au) as a function of temperature without any incident light. (b) Theoretical (purple line) and experimental (yellow circles) data of the optically induced change in temperature as a function of nanowire width, measured at 300 K. The greatest change in temperature occurs when the laser is on resonance with the width of the device. Image taken from Herzog, *et al.* (2014)[3].

1.3.4 Thermoplasmonics

Thermoplasmonics, or the study of plasmonic heat generation and dissipation in metal nanostructures, is a research topic of great interest[57, 58, 59, 60]. Research has focused on both minimizing loss due to resistive heating in optoelectronic devices as well as optimizing its production for a wide variety of applications, most notably in drug delivery[61, 62, 63] and steam generation[64].

Optically induced heating in nanowire antennas has been studied extensively[65, 66, 67, 68]. Recently, Herzog, *et al.* (2014)[3] investigated plasmonic heating in

nanowires in an extended electrode geometry where resistive heating can be measured directly from changes in differential conductance. Under continuous laser illumination, direct absorption and the excitation of surface plasmon modes in the nanowire heats the device, increasing its resistance. The increase in local temperature can be backed out from this change in resistance using Equation 1.4, derived from Ohm's law:

$$\triangle T = \frac{-R^2 \triangle G}{\frac{dR}{dT}} \tag{1.4}$$

where ΔG is the measured change in conductance, R is the resistance of the device, and the variable $\frac{dR}{dT}$ has been measured experimentally to be 0.12 for the Au bowtie nanowires in this thesis, consistent over many devices (Figure 1.4a). Using this value, bare nanowires at room temperature are found to increase in temperature by several Kelvin, depending on the geometry of the device. This effect can be much larger at low temperature, on the order of 10 K.

The resultant hotspot in differential conductance is localized to the nanowire. Fabricating nanowires beyond the full width at half maximum over the laser spot demonstrates that the heating occurs wherever the surface plasmon modes exist. Further, the polarization dependence of device response follows the expected dipolar shape discussed in Section 1.3.2, with maximum response at $\theta = 90°$. This indicates that the heating in the nanowire occurs in part due to the excitation of the structure's transverse plasmon mode.

1.3.5 Quantum Dots

In this thesis, the term "quantum dot" (as well as "nanocrystal") refers small pieces of single crystal semiconductor fabricated and employed in aqueous solution, although it can also refer to any solid state region of space where excitons are confined in three dimensions. Quantum confinement accounts for the tunability of quantum dots: when the radius of a nanocrystal is on the order of or less than it's exciton Bohr radius ($\lesssim$ 10 nm) the available energy levels split into discrete states and can be described as a particle in a box. Decreasing nanocrystal size increases confinement and therefore blueshifts its bandgap energy (Figure 1.5)[4].

Nanocrystals have the advantage of being near defect free and easy to fabricate in solution, making them an ideal candidate as active optical elements in nanoscale photonic devices. Nanocrystals typically need surfactants to be stable in solution, especially in polar solvents such as water. Choosing an appropriate solvent and ligand is crucial toward making effective use of quantum dots in solid state applications. In optoelectronic devices finding a suitable ligand is often difficult: for electronic measurements it should be short and fairly conductive to ensure decent coupling to electrodes, but it should be long enough to allow for efficient creation of excitons within the dot. However, shorter ligands will typically make nanocrystals less stable in solution.

Solution-cast quantum dot photosensitive devices have been fabricated through a number of experimental methods. However many of these studies rely on spincoating

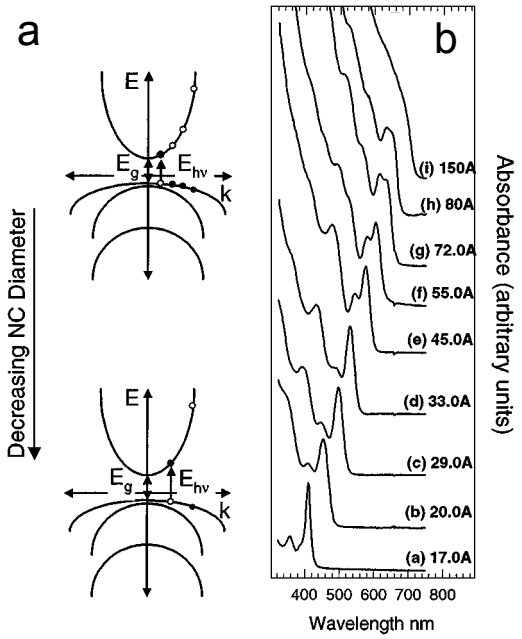

Figure 1.5 : (a) An energy diagram (E vs. k) of quantum confinement in nanocrystals. As the nanocrystal diameter decreases, the first allowed value for the wave vector k increases as does the separation between allowable k values, blueshifting its absorbance spectrum. (b) Experimental absorbance spectra for monodispersed nanocrystals over a range of diameters. Well-defined absorbance peaks indicate discretized energy states. Image take from Murry, *et al.* (2000)[4].

and top-down lithographic methods[35, 36, 37, 38, 39, 69, 70, 71] or are fabricated through laborious epitaxial techniques or with layered deposition of multiple materials, often organic, with highly dispersed quantum dots where the electrical cross sections are small enough for a single quantum dot to be addressed[72]. Dorn, *et al.* (2008)[39] and Prins, *et al.* (2012)[37] are the two experiments most relevant to the topics covered in this thesis. In the first, the authors present nanocrystal electro- and photoluminescence of CdSe/ZnS core/shell nanocrystals drop-casted onto In/Pt electromigrated nanojunctions. Due to the work function offset between the two electrodes, the Pt electrode injects predominately holes into the nanocrystals located between the nanogap, while the In electrode injects predominately electrons, facilitating excitonic recombination inside the nanocrystals. In the second experiment, PbSe quantum dots are deposited onto very wide (10 μm) self-aligned nanogaps using a dipcoating technique and the electronic and optical response of the resultant devices are studied in depth. The authors report remarkably high external quantum efficiencies of over 30 electrons-per-photon at 1.5 V. However, the paper makes explicit mention of the fact that it does not take any possible plasmonic field enhancement into account. Thinner electrodes, less than 300 nm in width, would move their structures closer onto resonance with the laser wavelengths used in their paper (near-IR to IR). This could potentially increase device efficiency and require less source-drain bias for efficient light detection.

The plasmon resonant electrodes of bowtie nanogaps are ideal for a wide array

of experiments with quantum dots where field enhancement would be useful, namely SERS, surface-enhanced fluorescence, and plasmon-assisted photocurrent generation. Metal-single nanocrystal-metal devices could also potentially serve as single photon sources[73] as well as opening up the possibility for understanding coupling between individual plasmons and excitons[74].

1.4 Sample Fabrication

All devices in this thesis are fabricated on n-type Si wafers with a 200 nm thermally grown oxide layer. Electron beam lithography is used to define the nanowire constriction and small triangular electrodes which extend to larger, prefabricated Au contact pads deposited using a shadowmask. After development, a 1 nm Ti adhesion layer and 13 nm of Au are deposited by electron beam evaporation, followed by lift-off in acetone. Nanowires are patterned to be 600 nm long and vary from 80 nm to 140 nm wide depending on the desired geometry.

In the case of "self-aligned" nanojunctions, an extra step of lithography is needed to create the gap[27]. In the first step, the left half of the nanowire is patterned and the 1 nm / 13 nm Ti/Au combination is deposited, followed by a 1 nm layer of SiO_2 and 14 nm layer of Cr. After the metal deposition, exposing the sample to air creates a layer of Cr-oxide which swells to extend just past the edge of the pattern, acting as a shadowmask in the second evaporation. The layer of SiO_2 prevents Cr and unwanted elements of the Cr etchant (namely cerium) from contaminating the

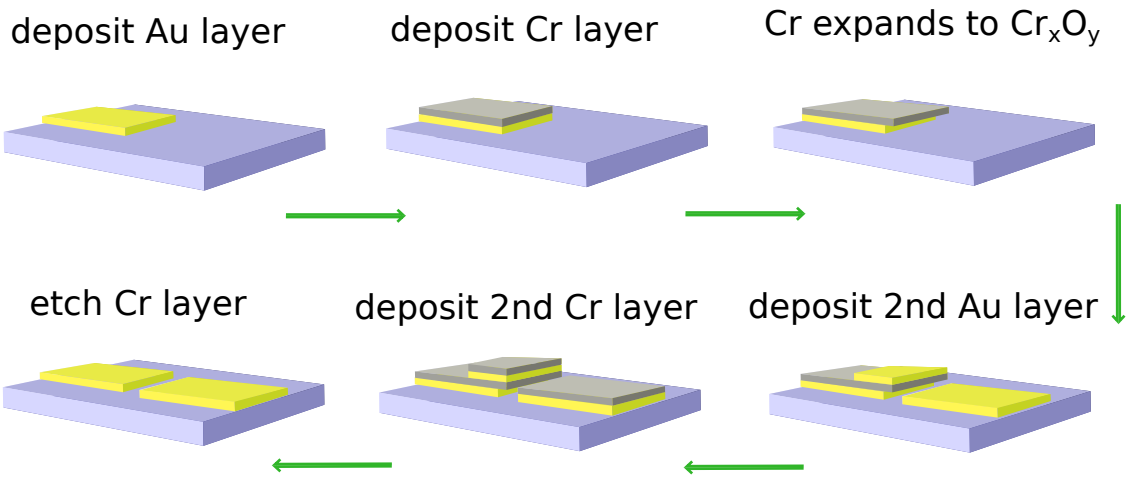

Figure 1.6 : A schematic of the self-aligned fabrication process. After the first lithographic step, a layer of Cr on the left electrode expands to Cr-Oxide to create a shadow mask for the right electrode.

Au and potentially degrading device plasmon response. During a second lithographic step, the right half of the pattern is aligned to the existing left half. An identical evaporation follows with the same materials and thicknesses. The Cr and SiO_2 are etched away, leaving a 2-10 nm gap between the two sides of the nanowire where the oxidized Cr expanded beyond the first pattern (Figure 1.6). The width of the gap can be tailored by adjusting the thickness of the Cr layer. The devices are then cleaned with O_2 plasma and wirebonded to a chip carrier.

Chapter 2

Plasmonic Optical Trapping

This chapter presents work from my Master's thesis. No new data are presented, but an in depth discussion of the challenges faced during the execution of the experiment, namely effective ligand chemistry and a suitable nanocrystal detection scheme, has been added. This goal of this project was to use the large electromagnetic fields generated in bowtie nanojunctions as an optical trap for nanocrystals in solution. A plasmonic trap would provide a clean method for isolating single to few quantum dots within junction nanogaps. Then, after removing the sample from solution, successfully trapped nanocrystals could be used as active optical and electrical elements for studying conduction and photoabsorption and emission of single to few quantum dots. Contacting isolated single or small clusters of quantum dots via traditional electron beam lithography is difficult due to the small size of most nanocrystals, and this method would provide a clever solution to an longstanding problem.

2.1 Theory of Optical Trapping

Optical trapping is a widely-used, non-invasive technique for manipulating dielectric objects on a submicron lengthscale. The force applied by the optical field is described by a surface integral over the volume of the object, given by:

$$\left\langle \vec{F} \right\rangle = \int_{\partial V} \left\langle \overleftrightarrow{T}\left(\vec{r},t\right) \right\rangle \cdot \vec{n}\left(\vec{r}\right) da \tag{2.1}$$

where,

$$\overleftrightarrow{T} = \left[\varepsilon_0\varepsilon\vec{E}\vec{E} - \mu_0\mu\vec{H}\vec{H} - \frac{1}{2}\left(\varepsilon_0\varepsilon E^2 + \mu_0\mu H^2\right)\overleftrightarrow{I}\right] \tag{2.2}$$

is Maxwell's stress tensor, $\vec{n}\,(\vec{r})$is the unit vector normal to the surface, and $\overleftrightarrow{I}$ is the identity matrix. In conventional laser trapping, implementing the Rayleigh approximation (Equation 2.3), where the trapped particle is much greater in size than the wavelength of the laser, reduces this equation to:

$$\left\langle \vec{F} \right\rangle = \frac{\alpha}{2}\nabla\left\langle \left|\vec{E}\right|^2 \right\rangle \tag{2.3}$$

where $\alpha$is the polarizability. Since the force goes as the gradient$\left|\vec{E}\right|^2$, it will be greatest where the gradient is the highest, i.e., at the focused waist of the laser beam[33]. This technique has been used extensively in the biological sciences[75, 76].

Plasmonic optical trapping relies on the localized electric fields generated by the evanescent fields in patterned metallic nanostructures to produce the necessary gradients for trapping. Under resonant laser illumination, the spatial extent of the electromagnetic field gradients in plasmon active structures are independent of the laser. Therefore, the trapping volume is not diffraction-limited as it is in traditional laser trapping, providing a method for subwavelength control of nanoscale objects[77]. Plasmonic optical trapping of nanoparticles has been repeatedly demonstrated over the past decade, but detection schemes on subwavelength length scales remain challenging. Additionally, the most recent experimental work in plasmonic optical trapping has been either restricted to the micrometer scale or proof-of-concept demonstrations of truly nanoscale trapping, without an explicit application [13, 14, 15, 78,

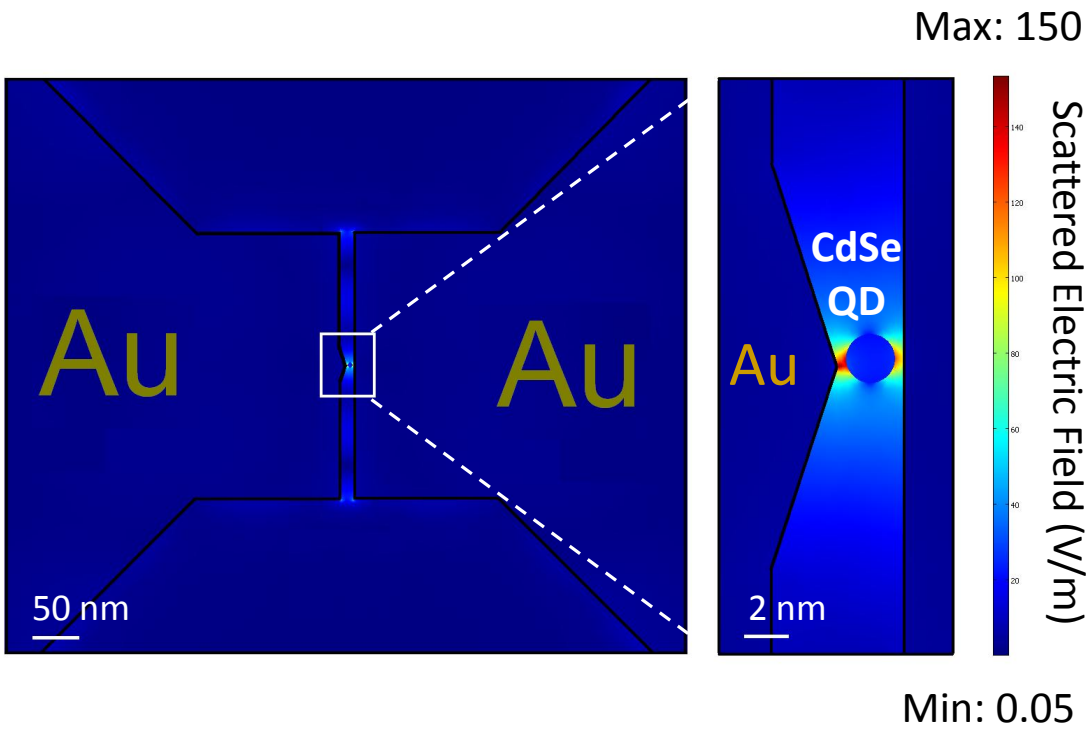

Figure 2.1 : An xy slice of the three-dimensional scattered electric fields in COMSOL. The maximum field enhancement is approximately a factor of 100 close to the tip of the inner gap (shown in red). The right panel is a close zoom of the area directly surrounding the nanocrystal.

75, 79, 80, 81, 82, 83]. Parallel device fabrication from solution via optical trapping in pre-patterned plasmonic devices from bulk solution could potentially allow for serial fabrication of subwavelength optoelectronic devices. This experiment aims to use the strengths of plasmonic optical trapping to integrate sub-10 nm nanocrystals into functional photodetective and photoemissive devices.

2.2 Numerical model for plasmonic optical trapping in nanogaps

The trapping forces on nanoparticles in and around the gap were calculated using a finite element method commercial solver (FEM, COMSOL 3.5a). A highly idealized nanogap was drawn in three dimensions, consisting of an interelectrode distance of 16 nm with a sharp tip extending 8 nm on one inner electrode face, positioned in the center. The junction includes the start of the macroscopic gold pads, with wavelength dependent dielectric values given by Johnson and Christy (1972)[7]. The gold electrodes are 15 nm thick, typical of the devices used in this study. The structure was illuminated with a plane wave parallel to the axis of the junction at the wavelength of our excitation laser, 1060 nm, and the scattered electric fields were calculated. The model was placed in a solution space filled with water ($\epsilon_r = 1.77$), but was left without substrate due to the computational complexity of the model. Previous calculations performed in the Natelson lab have demonstrated that its exclusion does not significantly impact the resulting fields in this geometry. Finally, a dielectric sphere, 4 nm in diameter with a dielectric constant of $\epsilon_r = 9$, was inserted and moved iteratively around the gap in each of the three spatial dimensions (Figure 2.2).

To calculate the trapping force on the nanoparticle at each position, the resultant electric fields were imported into MATLAB and where the force on the nanocrystal was calculated using the two methods described above: in the Rayleigh approximation and using the full Maxwell's stress tensor. In the Rayleigh approximation, where the particle is much smaller than the wavelength of incident light, the force is proportional

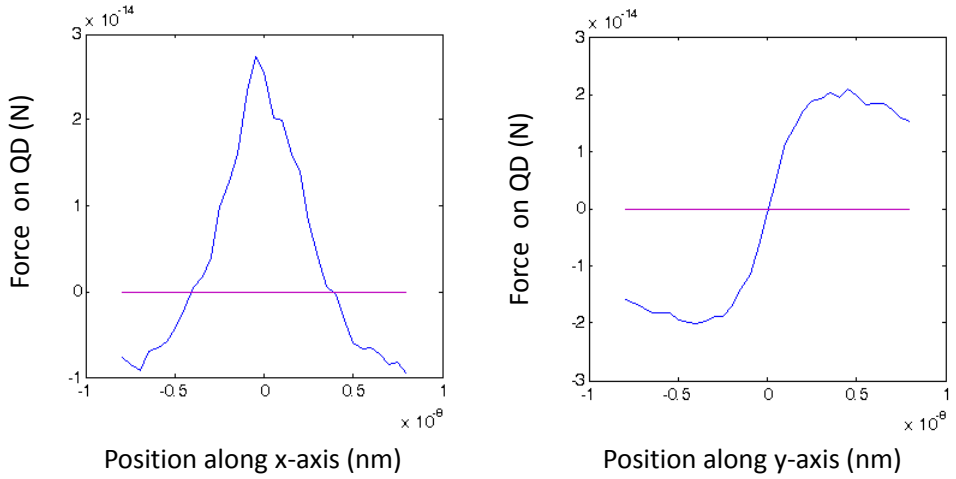

Figure 2.2 : The force on the nanoparticle as a function of distance away from the center of the tip using the full Maxwell's Stress Tensor formalism. The results match what would be most intuitive; the force is largest along the x-axis (parallel along device axis) closest to the tip, whereas the force changes polarity along the y-axis (parallel along gap axis), pulling the nanoparticle back toward the center of the gap. Here, the incident electric field is underestimated to be$E_0 = 1x10^5 \ \frac{\mathrm{V}}{\mathrm{m}}$.

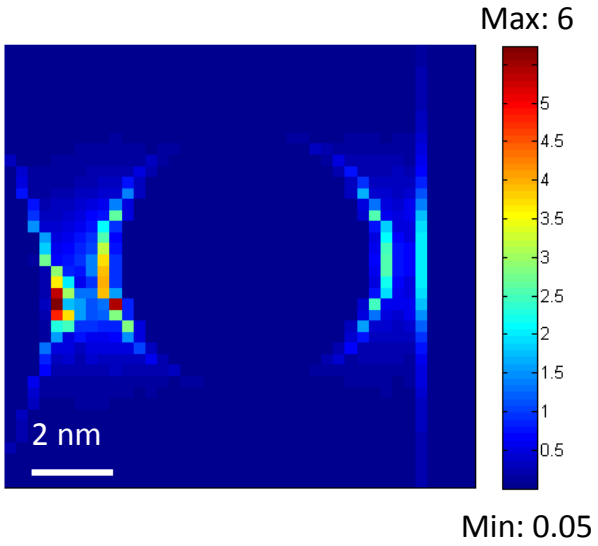

Figure 2.3 : An xy slice of the forces generated discrete points in the Rayleigh approximation. The colorscale is in femtonewtons, which summed over the entire spherical nanocrystal estimates the resultant force to be approximately 20 pN in this system for an incident electric field of $E_0 = 1x10^7 \frac{\mathrm{V}}{\mathrm{m}}$.

to the gradient of the electric field squared. To do this, the fields in and around the dielectric sphere were re-meshed into small pieces, and the force was calculated at each mesh point using Equation 2.3. The total force on the sphere was then calculated by summing all force matrices located within the sphere. This method allows for an intuitive visualization, displaying the magnitude of the force at each point on the nanoparticle (Figure 2.3). The maximum force generated in this idealized system was approximately 20 pN.

However, since the nanoparticle is comparable in size to the trapping volume, the Rayleigh approximation only provides a rough estimate of the force and the full

Maxwell's stress tensor is needed. The Maxwell's stress tensor involves an integral over the surface of the nanoparticle (Equation 2.2), which can be computed in COMSOL and similarly exported into MATLAB for further analysis. As expected, the resultant force depends considerably on the incident laser power and the gap geometry. The IR laser used in this experiment is approximately 100 mW, which, for a diffraction limited spot size of approximately 1 μm, rounds out to an average power per unit area of $\langle S \rangle = 8x10^3 \ \frac{\text{kW}}{\text{cm}^2}$, or an incident electric field of approximately $E_0 = 1x10^7 \ \frac{\text{V}}{\text{m}}$. Optimizing gap geometry, the trapping force can reach into the tens of piconewtons in the gap for this numerical model. This calculated force is large enough to overcome the approximate force due to Brownian motion for a particle of that size, given by $\frac{kT}{d} = 0.5$ pN, where d is the diameter of the particle, here assumed to be 4 nm. Due to the highly idealized nature of the model, these values are merely proof-of-concept theoretical estimations. Nevertheless, the order-of-magnitude numerical calculations established roughly what laser power would be necessary to generate the appropriate electric field enhancement for suitable trapping fields.

2.3 Experimental attempts at plasmonic optical trapping

Samples were fabricated using the method described in Section 1.4, wirebonded to a 16-pin DIP chip carrier, and loaded into an open air breakout box. Devices were electromigrated to an open circuit resistance value, following the procedure laid out in Section 1.3.2. This method assured than any measurable conductance post trapping

can be attributed to some form of change to the junction due to the quantum dot solution. The final conductance of each junction was then recorded using a lock-in amplifier and current preamplifier (Figure 2.4).

Several drops of quantum dot solution are place on top of the sample inside the chip carrier, forming a small droplet, which allows for approximately half an hour of consistent trapping. The droplet effectively acts as a lens for the laser light, so drop placement and maintenance is crucial to this process; if the droplet is too spherical the laser can be distorted past a visible focal point, but with too little solution the liquid evaporated quickly and dots would crash out of solution onto the sample, rendering it useless.

In other trials, samples post-breaking were debonded and put into a small PDMS flow cell, filled with nanocrystal solution, and capped with a coverslip. This allowed for longer trapping times, but didn't allow for the conductance of the junction to be monitored during the trapping process. The devices would then be rebonded and remeasured for any change away from an open circuit conductance.

Trapping was performed using a 1060 nm diode laser, near the theoretically-calculated resonance of traditional nanogaps explored previously in our lab[8]. The sample was translated using a micrometer stage and each device is exposed to focused IR laser light while the conductance was monitored. During this process discrete state switching was observed in previously open junctions, induced after a short (the delay can range anywhere between immediate and several minutes) period of laser exposure

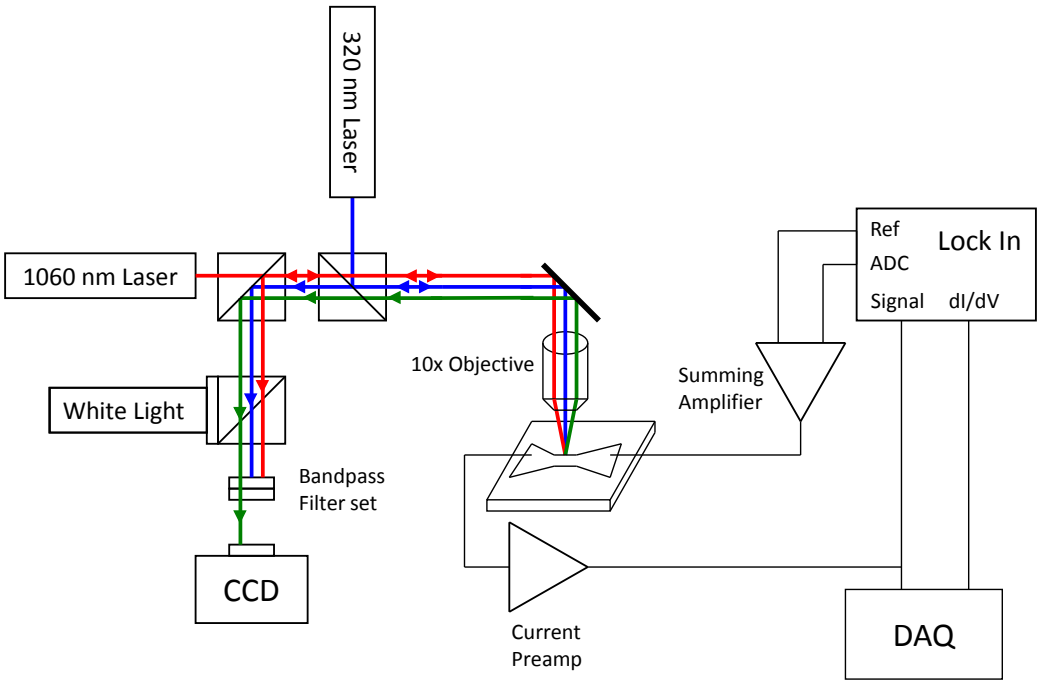

Figure 2.4 : A diagram depicting the optical and electronic apparatus. A NI-DAQ is used to electromigrate junctions to negligible conductance. After migration, current and conductance ($\frac{dI}{dV}$) are swept as a function of source-drain bias using a lock-in amplifier. For IV sweeps the lock-in sources a small ac voltage which is summed with a dc voltage sourced from a DAC port on the back of the lock-in. The dc current is measured with a corresponding ADC port and the $\frac{dI}{dV}$ is measure on the front panel with respect to the same reference signal. Trapping and fluorescence measurements are integrated into the same apparatus, using a straightforward optical setup and a 50 $\times$ long-working distance objective.

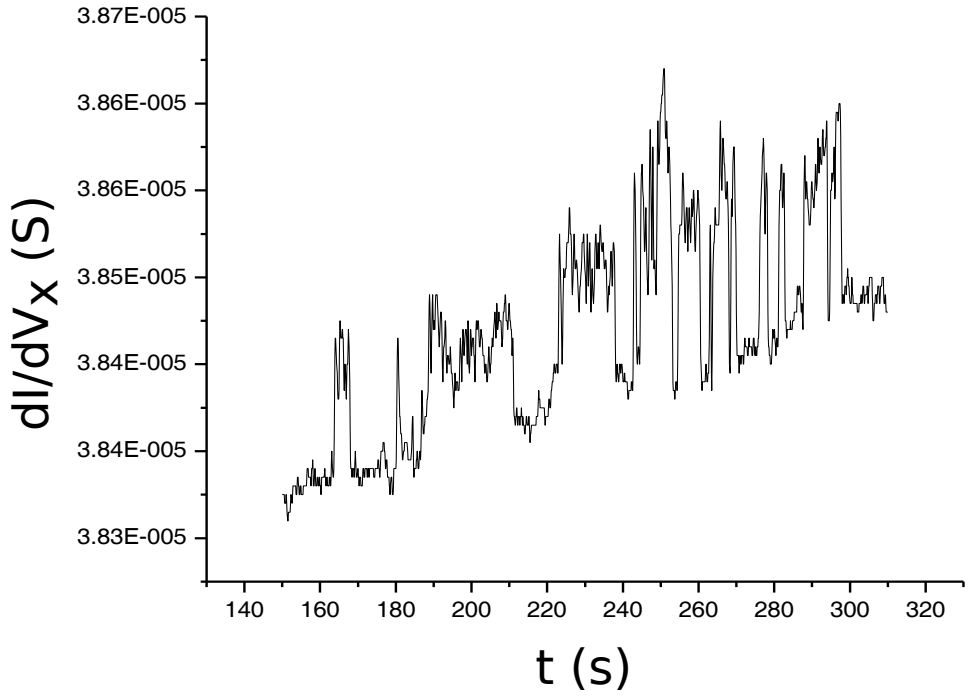

Figure 2.5 : A plot of conductance a nanogap during optical trapping demonstrating typical conductance state switching indicative of a possible trapping event, quantum dots moving through the gap, or a quantum dot(s) rearranging itself within the gap.

(Figure 2.5). Switching can continue after the laser is shut off, indicated that the laser is most likely responsible for bringing nanocrystals near the gap, and the nanocrystals continue to rearrange themselves after a trapping event(s) occurs. Additionally, at high enough concentration and laser power, nanocrystals can be seen aggregating under the laser, and the large bundles can be visibly dragged and positioned on the surface.

Resistance measurements on "successful" devices were typically in the 10 kΩ - 1 MΩ range and predominantly linear in voltage. Slight curvature in some devices'

IV characteristics could be indicative of low-resistance tunneling across quantum dot aggregates. Devices are typically highly instable and degrade after several IV sweeps. Photoconductance measurements in the resultant junctions are even more delicate; the quantum efficiency of the junctions with successful trapping events is so low that it requires extremely high UV laser power and high current-to-voltage gain. Photocurrent in these structures has been observed in several different devices, typically with values on the order of 10 nA for full incident laser power on the order of tens of milliWatts focused onto the junction.

These experiments were performed over the course of two years on several hundred devices. However, successful trapping events only been observed within the last three months with the right combination of laser power, optical alignment, electronic sensitivity, and nanocrystal size and coating. With fourteen total devices per chip, typical yields are approximately 10% (i.e. 0-2 devices per chip). Finally, several control experiments were performed in which trapping was performed in plain DI water, with no notable conductance state switching, as well as searching for photocurrent in bare junctions. In this case, the photocurrent observed was two orders of magnitude below that of the nanogaps with trapped nanocrystals.

2.4 Challenges with nanocrystal quantum dots

There were two primary challenges in realization of this experiment: finding an effective measure to get quantum dots to stick to the Au after trapped near the gap,

and post-trapping verification that a trapping event had occurred. A wide range of combinations of ligands and solvents were employed during trapping trials, supplied in large part by the Wong group at Rice.

A short ligand terminated with a thiol group (-SH) pointing away from the dot would be ideal, as thiol groups are know to bond strongly with Au. However such a ligand is difficult to implement because short thiols are typically very reactive and have a strong affinity for the dots, as well as other thiol groups (in the case of dithiol ligands). Ligand exchanges from more traditional molecules to dithiols in CdSe nanocrystal solutions resulted their crashing out of solution. Pyridine ligands were the next best option because they are short and relatively conductive. However, they were also fairly quick to aggregate together in solution (on the order of hours), especially in water, making extensive trials with pyridine ligands difficult. Oleic acid is a standard ligand for CdSe nanocrystals, but it is long and known to be electrically insulating, so it was not a good choice for this application. The quantum dots with the most success were commercially purchased from cYtodiagnositics (http://www.cytodiagnostics.com/). The nanocrystals used were 5 nm in diameter, CdSe/ZnS core-shell nanocrystals functionalized with an amine (-NH_2) coating, suspended in water (the exact ligand used was not disclosed by the company). This solution was chosen in large part because the solution was stable of over many months, making extensive trials without changing too many variables at once possible.

The pyridine, amine, and oleic acid ligands were used in combination with a va-

riety of solvents, from hexane and toluene, to less volatile solvents like water and trichlorobenzene. Using water as a solvent has the advantage of a relatively slow evaporation rate compared to other typical nanocrystal solvents (toluene, hexane, etc.) as well as being chemically inert with respect to our prefabricated metal structures. However, water has remarkably high surface tension which could interfere with trapping.

Submerging the sample in solution for long-term trapping experiments was a consistent problem. Either method employed in Section 2.3 presented a series of difficulties, even with water and trichlorobenzene. Dropping and replenishing the droplet of the solution in the chip carrier before it evaporated entirely during the experiment (the most successful procedure) often changed the focal point of the laser spot and had to be constantly readjusted. In other trials, forming a sealed volume of either water or tricholorobenzene also proved challenging; in order to get the sample into a water-tight cell, it had to be debonded, making electrical detection techniques for trapping impossible. Removing the sample from solution in either case often generated quite a bit of surface contamination and it was typically difficult to keep the solution of depositing lots of nanocrystal aggregates onto the surface throughout the experiment, regardless of the choice of solution or its concentration. Too much rinsing or sonicating after a trapping experiment appeared to remove all of the dots rather than selectively keeping nanocrystals that had bonded to the Au surface.

The second problem was detecting if any nanocrystals had been trapped and

remained in or near the gap. Using a combination of fluorescence or electronic measurements would be ideal. However, fluorescence imaging of single to few quantum dots proved to be difficult. Determining quantum dot location via SEM was also difficult because the dots appear very faint in SEM micrographs, if they appear at all, since they are not metallic. Electronic characterization of previously open circuits, which demonstrated conductance switching discussed above, was the only reliable metric found to provide any evidence that a trapping event had occurred.

In short, preferential and robust bonding of trapped nanocrystals to Au rather than clumping together on the surface of Au or SiO_2 was never routinely achieved. If the nanocrystals had bonded, it was most likely in aggregates near the nanogap, and not chemical bonds between individual dots and the Au surface. Due to the difficulty of trapping and post-trapping characterization, several other methods of depositing quantum dots onto nanogaps were tried. In the first, a monolayer of a dithiol group (1,4-butanedithiol and 1,6-hexanedithiol were both tried) was assembled on the surface of the Au electrodes as a method to potentially self-assemble nanocrystals onto the surface. After depositing the SAM, the samples were soaked in pyridine coated nanocrystals overnight and rinsed thoroughly in chloroform. Again in this case, there was trouble discerning if quantum dots had bonded effectively to the SAM, or if the nanocrystal ligand had thwarted any chemical interaction between it and the underlying thiol group. XPS was used to tell if any nanocrystals had bonded to the SAM. From the results, it appeared as though there was a thin, non-uniform coating of

nanocrystals but none of the resultant film-nanogap devices had measurable electrical or optical responses after the deposition. This result could come from the fact that SAMs with shorter dithiol molecules often "lie down" instead of "standing up" to make their second thiol group available for bonding. Alternatively, had some nanocrystals bonded to open thiol sites, the thiol groups and nanocrystal ligands together might still have been too long and electrically insulating to push current through.

In the second experiment, quantum dot films were deposited by opening a several micron by several micron wide windows in PMMA on top the nanogaps using electron beam lithography following the work of Mentzel, *et al.* (2012)*[84]*. Nanocrystals in hexane were then flash evaporated over the entire sample, drying on the surface only where there were lithographically patterned windows. The PMMA was then stripped away using acetone leaving nanocrystal films in well-defined areas. This method was much cleaner than the dithiol assembly or the trapping experiments, and the films were imageable using a fluorescence microscope. However, these films were still very resistive and did not ever produce any measurable photocurrent.

Chapter 3

Plasmon-assisted photoresponse in bowtie nanojunctions

To avoid many of the problems we experienced working with nanocrystals, but still examine plasmon-based photodetection, we turned to a more controlled absorber material: amorphous Ge. Uniform amorphous Ge films could be readily deposited via electron beam evaporation, making regular photocurrent trials possible. This chapter is an adapted version of a paper recently accepted to ACS Photonics[85].

Light coupled into surface plasmons in metallic nanostructures can generate extremely large enhancements to the local electromagnetic field. Optical antennas exploit the resonant behavior and large scattering cross section of plasmons in nanostructured metals for use in a wide variety of applications including surface-enhanced Raman spectroscopy (SERS)[9, 10], subwavelength optics[11, 12], plasmonic optical trapping[13, 14, 15, 16], and plasmon-assisted light harvesting[17, 18, 19, 20, 21, 22, 54, 55, 56]. Photosensitive devices utilizing plasmonic nanoantennas generate photocurrent through two dominant mechanisms: Near-field photons can be absorbed in a nearby semiconductor to create electron-hole pairs; or high-energy ("hot") electrons generated by the plasmon can tunnel across a semiconductor-metal potential barrier, directly resulting in photocurrent. Plasmonically active devices often have the benefit of being highly polarization dependent, operational at small biases, and capable of

being fabricated with photoactive elements on a scale smaller than the wavelength of the incident light.

Gold "bowtie" nanojunctions, consisting of a nanowire (with or without a nanogap) connected by two extended leads, have been shown to act as combined optical antennas and electrical probes[25]. The plasmon response in this geometry is dominated by a transverse dipolar mode, resonant for incident light polarized perpendicular to the length of the constriction. In devices with nanogaps at their center, made through either electromigration or via a multi-step "self-aligned" lithographic technique[27], the transverse plasmon mode hybridizes with multipolar "dark" modes at the gap edges to form a strong electromagnetic field enhancement at the junction center, or "hotspot". The SERS response of molecules assembled into these hotspots follows the signature polarization dependence of dipolar optical antennas, with maximum response perpendicular to the axis of the constriction[1]. This is in contrast to expectations of the nonresonant "lightning rod" effect, when the maximum plasmon response occurs when the incident polarization parallel to the elongated direction of a metal wire or tip, from the excitation of longitudinal or tip plasmons[33].

In no-gap bowtie nanowires, resonant laser illumination produces a polarization-dependent hotspot via photothermally induced changes in resistivity[3]. Direct absorption and the excitation of the transverse plasmon mode locally increase the temperature of the nanowire, decreasing its conductance, $-\Delta G$, due to the temperature-dependent resistivity of the metal. The polarization dependence of this change is also

dipolar, so that the temperature of the nanowire increases more for the transverse excitation, even without the existence of gap plasmons. This measurement provides a convenient measurement technique to assess the plasmon response of the nanowire material itself.

In this work, we study the photoresponse of bowtie nanoantennas overlaid with a thin Ge film. We examine the plasmon-assisted photoconduction (I_{photo}) in bowties with nanogaps. At low Ge thicknesses, we find that the photoconductance is maximal with incident polarization transverse to the nanowire; in contrast at higher Ge thicknesses, the maximum photoconductance occurs when the incident polarization is rotated by 90°. The Ge thickness alters which plasmon response is dominant in the nanogaps, the resonant transverse mode (at low thicknesses) or the nonresonant "lightning rod" response (at high thicknesses). A concern is whether the transverse plasmon mode is eliminated entirely due to degradation of the Au properties with thicker Ge layers. To test for this, we also measured the plasmon-induced heating in unbroken (no-gap) nanowires. We find experimentally, and in accord with a computational model, that the presence of Ge predictably redshifts the resonance of the nanoantenna's transverse plasmon mode without degrading the Au plasmonic response.

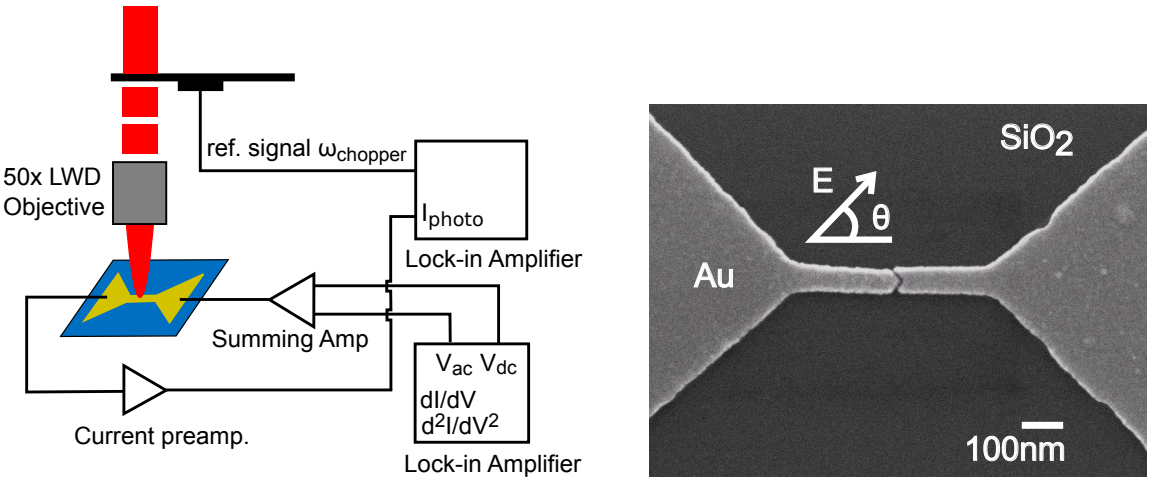

(a) (b)

Figure 3.1 : (a) A schematic diagram of the experimental setup. Devices are biased with a dc voltage summed with a small (typically 10 mV) sinusoidal ac excitation voltage. Signal passes through a current preamplifier to two separate lock-in amplifiers, one synched to the ac frequency to measure the first and second harmonic of the differential conductance and a second synched to an optical chopper to measure photoresponse. (b) An SEM image of a typical self-aligned device.

3.1 Methods

Each device is scanned with a 785 nm diode laser configured with a telescopic lens rastering system to create a spatial map of the photoresponse. The laser has a Gaussian beam profile with a full width at half-maximum of approximately 1.8 μm, operating in CW mode at a typical laser power of 3-4 mW reaching the sample. A lock-in amplifier, synched to an optical chopper at a frequency of 281 Hz, is used to measure device optical response: either the photocurrent generated in self-aligned devices (I_{photo}) or the optically induced change to the conductance in gapless nanowires ($\Delta G = {}^{\Delta I}/_{V_{dc}}$). The sample is biased with the summed output of the desired dc voltage, typically up to 0.2 V, and a 10 mV RMS ac voltage, and a second lock-in, at frequency 789 Hz, measures the first- and second-order differential conductance (${}^{dI}/_{dV}$ and ${}^{d^2I}/_{d^2V}$). The dc current (I_{dc}) is measured using a digital-to-analog converter (DAC) built into one of the lock-in amplifiers (Figure 3.1a). After each scan, the laser is then finely positioned at the hotspot center by maximizing $-\Delta G$ or I_{photo}, the polarization is rotated continuously from $\theta = 0°$ to $\theta = 360°$ (with $\theta = 0°$ defined to be along the nanoantenna long axis) using a motorized half-wave plate, and the optical and electrical responses are measured. Bare bowtie nanowires (with and without nanogaps) are coated with an amorphous Ge film of varying thickness deposited by electron beam evaporation, and remeasured using the same procedure. All measurements presented in this paper were conducted at room temperature at a pressure on the order of 100 mTorr.

3.2 Results

3.2.1 Photocurrent measurements

Early photocurrent measurements included both electromigrated and self-aligned nanojunctions overlayed with a 35 nm amorphous Ge film. Photoresponse in each case is dominated by a positive photoconductance of the Ge in the gap region. Photocurrent is linear with respect to laser power and dc bias, and only occurs at the junction center. Measurements on electromigrated junctions produced a wide range of polarization dependences for photocurrent in devices fabricated at the same time, on the same wafer, with identical lithographic exposure and development parameters. These plots often contained a relatively small $cos^2(\theta)$ angular contribution associated with optical antennas, inconsistent with previous SERS and optically induced heating experiments in these structures (Figure 3.2).

Varied polarization dependence of the photocurrent in electromigrated bowtie nanowires has been reported in nanojunctions made with graphene[42]. The authors of that work cite optical rectification as the source of photocurrent in their structures, but demonstrate similar resonance conditions (near-IR) and provide evidence for the specific nanoscopic configuration of the break-junction at the gap playing a major role the polarization dependence of its photoresponse.

In order to mitigate the effect of the local geometry of the nanogap, we started experiments on self-aligned nanojunctions, which are known to have more consistent device-to-device nanogap geometry and plasmon response. Photocurrent mea-

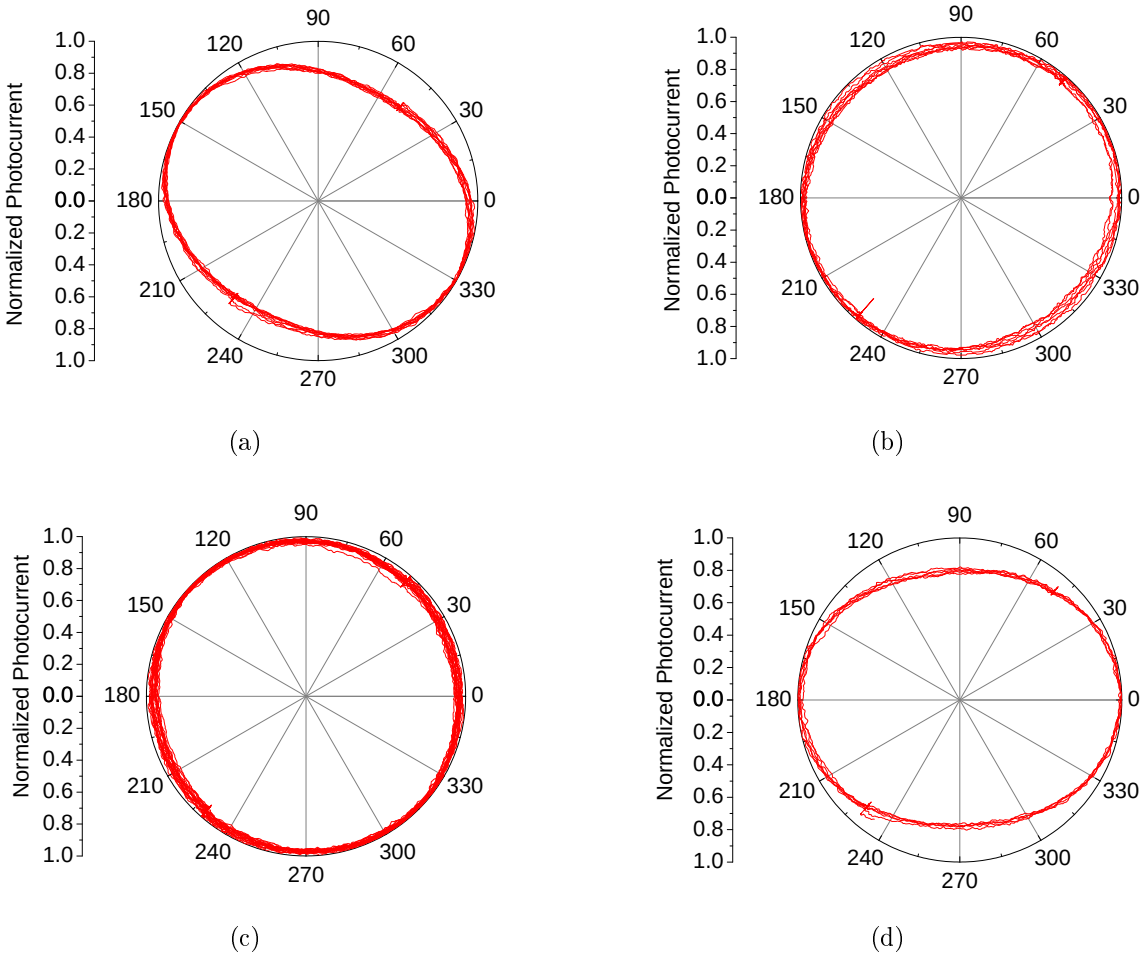

Figure 3.2 : Polarization dependence of the photocurrent in four separate electromigrated bowtie nanowires with a 35 nm amorphous Ge film evaporated after electromigration. All four devices were fabricated on the same sample using identical exposure and development parameters, and were broken using the same automated procedure. Photocurrent is measured over many angular sweeps ($\theta = 0-360°$) of the polarization of the incident laser light and normalized to the maximum of photocurrent value of each sweep.

surements of self-aligned nanojunctions with 130 nm widths and a 35 nm Ge film consistently produced polar plots with significant $cos^2(\theta)$ contributions and a maximum photoresponse at $\theta = 0°$ (Figure 3.3b). Photocurrent generated in self-aligned nanojunctions fabricated with a nanowire width of 80 nm and a 10 nm Ge film was found to be maximized at $\theta = 90°$ (Figure 3.3a), at striking 90° shift in polarization dependence.

To understand this, we consider the plasmons in the system. In previous work exploring photoresponse in bowtie nanoantennas, it has been demonstrated that the greatest field enhancement occurs when incident light is polarized perpendicular to the nanowire axis, corresponding to a strong dipolar transverse plasmon mode. For bare Au nanowires, this mode is known to be resonant at 785 nm for bare nanowires $\sim$ 130 nm wide and 13 nm thick. Here, the presence of the Ge film redshifts the resonance of the transverse plasmon mode away from 785 nm so that the dominant plasmon response occurs via the remaining longitudinal, "lightning rod" mode. Fabricating skinnier nanowires ($<$ 100 nm) moves the transverse mode roughly back onto resonance at fixed laser wavelength.It would appear that in the narrower-wire nanogap devices with the thinner Ge film, the photocurrent is dominated by this transverse plasmon response, while for the wider-wire nanogap devices with thicker Ge the dominant plasmon response is that of the nonresonant longitudinal "lightning rod" mode.

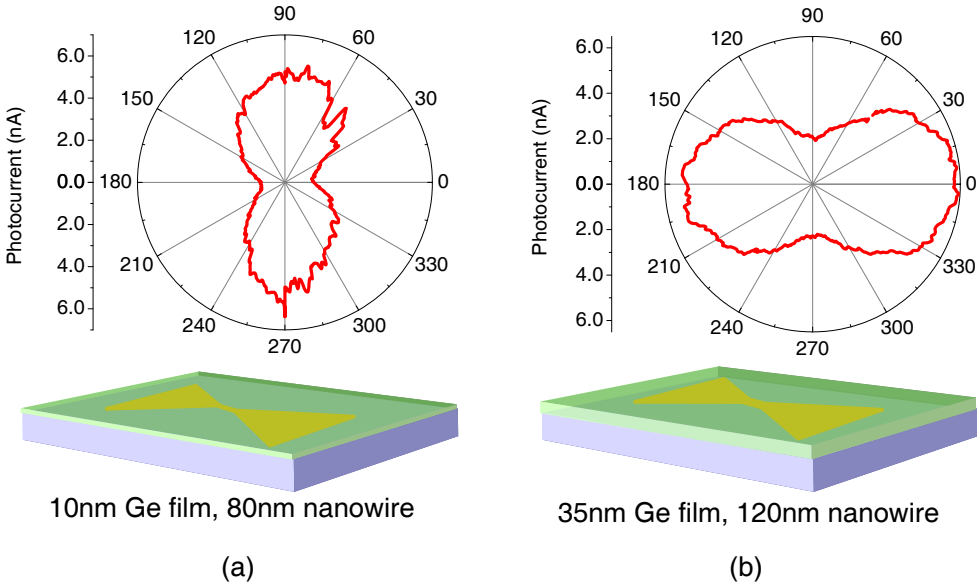

Figure 3.3 : (a) The dipolar polarization dependence of an 80 nm wide nanoantenna with a 10 nm Ge film where the transverse plasmon mode is roughly on resonance with the 785 nm laser. (b) The dipolar polarization of an 130 nm wide nanoantenna with a 35 nm Ge film where the "lightning rod" mode is roughly on resonance with the 785 nm laser.

3.2.2 Heating in Ge-coated nanowires

An issue is whether, in the thicker Ge devices, the plasmonic properties of the Au itself is degraded (e.g., through partial alloying with the Ge due to the longer deposition), or whether the change in the plasmon response is due purely to shifting of the resonant transverse mode away from the operating wavelength. To understand this dramatic change in nanogap device plasmon response, we fabricate "unbroken" no-gap nanowires, and assess the plasmonic properties of the Au through study the photothermally induced change in the conductance, $-\Delta G$ (due to the temperature-dependent Au resistivity), as a function of nanowire width and Ge film thickness. Measurements on bare Au bowtie nanowires ($\sim$ 130 nm wide and 13 nm thick) are consistent with previous work measuring resistive heating in these structures; the conductance change includes a characteristic $cos^2(\theta)$ polarization dependent contribution, with a maximum at $\theta = 90°$ due to the contribution to heating from the structure's transverse plasmon mode[3]. This indicates that the laser wavelength is on resonance with the transverse mode of the nanowire (width $\sim$ 130 nm, thickness 13 nm), heating it approximately by 2-10K depending on the exact width of the device and the incident laser power. The increase in temperature can be estimated directly from the change in conductance using the formula provided in Herzog, et. al. (2014), $\triangle T = \frac{-R^2 \triangle G}{\frac{dR}{dT}}$, where R is the resistance of the device and $\frac{dR}{dT} = 0.12$ for these Au bowtie nanowires. This value has been measured to be consistent for many nanowire devices.

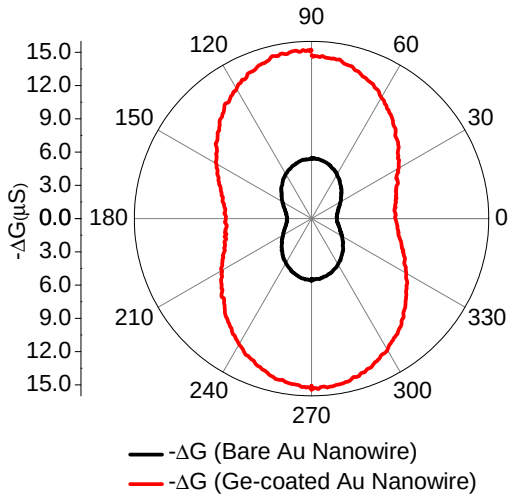

(a) 5nm Ge film

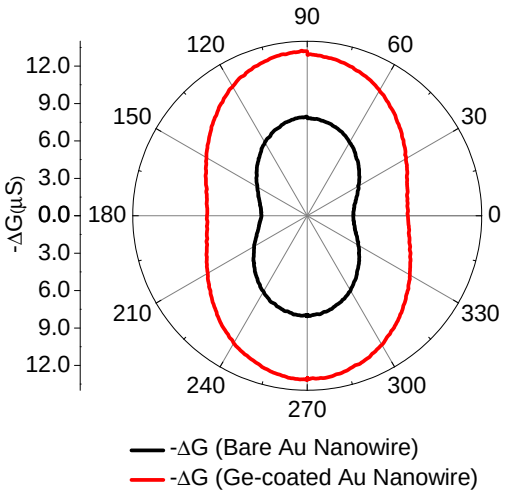

(b) 10nm Ge film

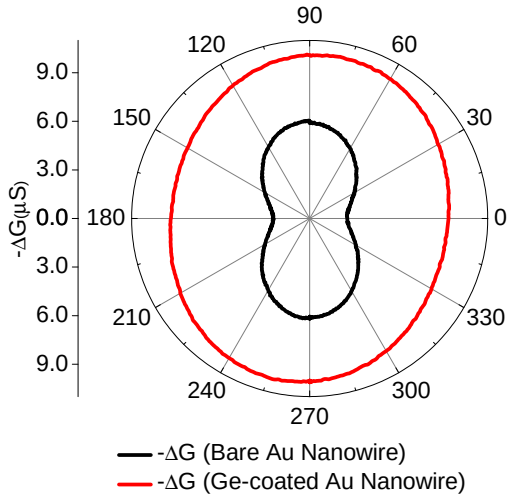

(c) 15nm Ge film

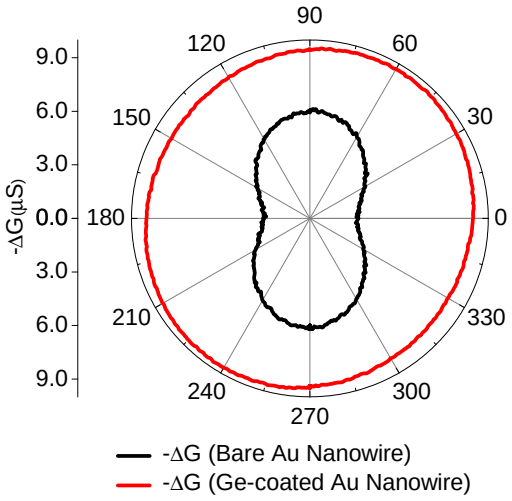

(d) 20nm Ge film

Figure 3.4 : Experimental data displaying the change in polarization dependence for "unbroken" nanowires with varying layers of Ge deposited on top. Each successive trial becomes more circular as the resonance of the transverse mode moves further away from the laser wavelength.

After each initial characterization of bare devices, a Ge film of varying thickness (5 nm, 10 nm, 15 nm, and 20 nm) is deposited by electron beam evaporation and the photoresponse is remeasured (Figure 3.4). For each trial, the polar plots become progressively more circular, as the increasing thickness of Ge redshifts the resonance of the transverse plasmon mode away from the laser wavelength of 785 nm. The data are fitted to the expression $-\Delta G\left(\theta\right) = \Delta G_0 + \Delta G_{plsm} cos^2\left(\theta\right)$. Here, ΔG_0 is the nonresonant, direct absorption contribution, while ΔG_{plsm} is the component of the conductance change due to dipolar plasmon-based heating. The ratio $^{\Delta G_{plsm}}/_{\Delta G_0}$ then gives a measure of the transverse plasmon contribution to the change in conductance for each thickness trial. This ratio is roughly constant for bare junctions across all four trials, but steadily decreases in the presence of increasing Ge film thickness (Figure 3.5a). By 20 nm of Ge, the devices lose all their polarization dependence; their polar plots become entirely circular, indicating that the presence of the film has shifted the transverse plasmon mode far off-resonance, removing the dipolar response of the nanoantenna, and leaving behind only heating from nonresonant absorption.

To verify that the dominant effect on the polarization is redshifting of the plasmon resonance rather than a simple attenuation of the plasmon resonance, we fabricated intentionally off-resonance nanowires, less than 100 nm wide, and then deposited a Ge film to redshift the resonance back to the laser wavelength. The pre- and post-Ge deposition bowties are analyzed following the above procedures (Figure 3.5b). In this case we see the $^{\Delta G_{plsm}}/_{\Delta G_0}$ ratio increase, indicating that the polarization dependence

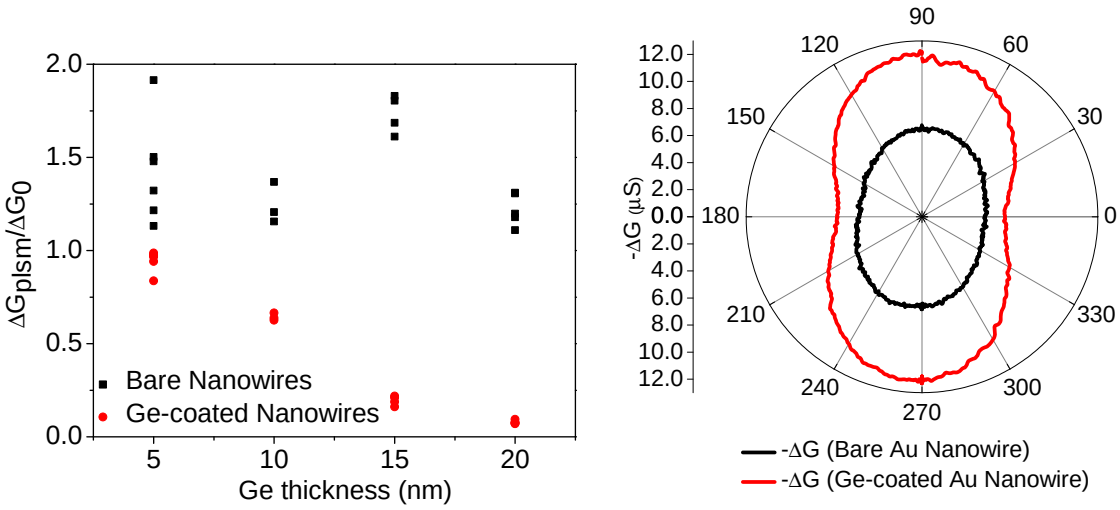

(a) (b)

Figure 3.5 : (a) Each point represents the ${}^{\Delta G_{plsm}}/_{\Delta G_0}$ ratio measured for an individual device, before and after the Ge film deposition. The values for bare nanowires (black squares, with each batch of bare wires marked at the Ge thickness eventually coated) are roughly all the same for all measured bare junctions, which vary in width from device to device. The values for Ge-coated nanowires (red circles) have decreasing ${}^{\Delta G_{plsm}}/_{\Delta G_0}$ ratios for increasing Ge thickness, indicating that their polar plots are more circular with less contribution of the transverse plasmon mode toward the total photoresponse. (b) A polar plot of an off-resonance, bare device moved closer to resonance with the addition of a 10 nm Ge film. In this case the ${}^{\Delta G_{plsm}}/_{\Delta G_0}$ ratio increases.

of the junction becomes more dipolar in the presence of the Ge film. This effect was found to be consistent in 8 measured devices.

3.2.3 COMSOL Modeling of Ge-coated nanowires

These experiments verify that for the gapped nanojunctions a 35 nm Ge film will remove the transverse plasmon mode's contribution toward the photocurrent for a device previously on resonance with the laser wavelength, as seen in Figure 3.3b. For structures made off resonance with the laser, adding an appropriately thick layer of Ge can tune the device back onto the laser wavelength, as seen in Figure 3.3a. To map out the appropriate thicknesses of Ge over a range of device widths, the resonance of the transverse plasmon mode in nanoantennas was modeled with a finite-element software package designed to solve differential equations over physical spaces (FEM, COMSOL 3.5a). A cross-sectional model was designed so that the incident light is polarized perpendicular (transverse magnetic mode) to an infinitely long nanowire, isolating the transverse plasmon mode for the purposes of this study (Figure 3.6a). Ge is known to be entirely amorphous when deposited by evaporation with the substrate at room temperature, and accordingly a dielectric function for amorphous Ge was used in the model[86, 87]. The dielectric function for Au was taken from Johnson and Christy (1972)[7]. Maxwell's equations are solved over the entire solution space as a function of nanowire width and Ge film thickness. For an incident plane wave with free space wavelength ranging from 400 nm to 1500 nm, a scalar proportional to the optically

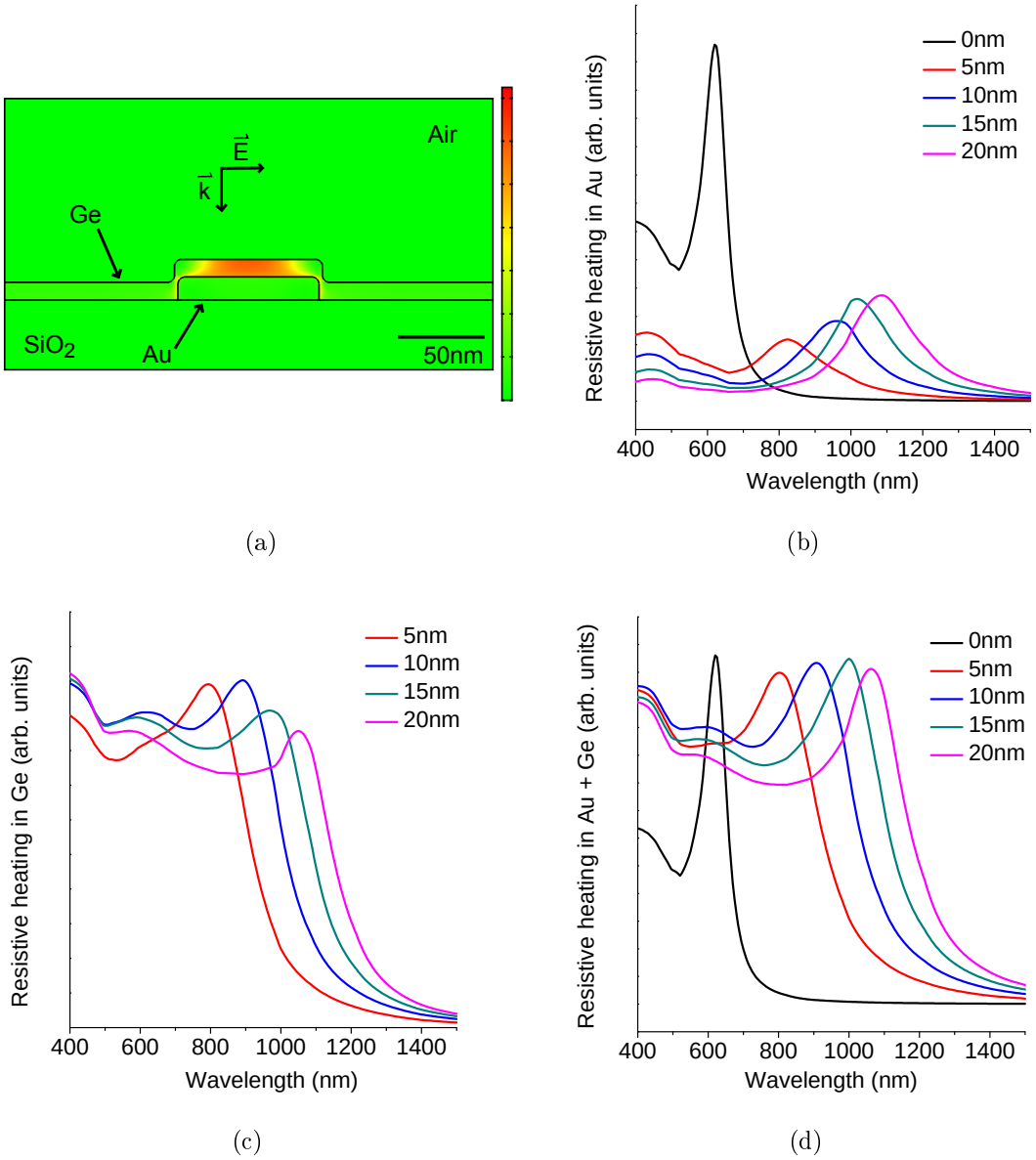

Figure 3.6 : (a) An image of the solution for the variable Q plotted in arbitrary units, green indicating zero heating. (b) Spectra of the variable Q for an 80 nm nanowire in the 2D COMSOL model for varying thicknesses of Ge. (c) Spectra of the variable Q integrated over a portion of the Ge for an 10 nm film on top of an 80 nm nanowire. (d) Spectra of the sum of the resistive heating in the Au nanowire and the Ge film.

driven resistive heating is found by integrating resistive heating $Q = \frac{1}{2} Re\left(\sigma \left\|\overrightarrow{E}\right\|^2\right)$ over the area of the Au, where σ is the electrical conductivity and $\left\|\overrightarrow{E}\right\|$ is the norm of the total electric field (Figure 3.6b). As the film thickness increases, the original resonance is redshifted and broadened, as expected from previous work exploring plasmon modes in the presence of semiconductors[55, 88, 89]. Bare devices with transverse modes previously resonant at the laser wavelength of 785 nm will be shifted off resonance further into the near-IR in the presence of a 5-10 nm film of Ge.

This simple model provides a proof-of-concept explanation for the shift in the resonance of the transverse plasmon mode, but does not take into account heating from absorption in the Ge layer; it assumes that all photothermally induced change in current comes from heating in the Au alone. This calculational omission accounts for the predicted decrease in the magnitude of the peaks for increasing Ge thickness not seen in the experiment. In contrast, in the measurements the photothermal heating in unbroken bowtie nanowires is larger with the Ge film than without it (i.e. ΔG_0 of the Au is always larger for Ge-coated nanowires than for bare nanowires). Integrating the variable Q over the volume of the Ge film produces a broad plateau at a wavelength below the plasmon resonance due to direct absorption in the Ge overlayer (Figure 3.6c). Adding the two spectra for Q together (i.e. Figure 3.6b + Figure 3.6c) results in resonance peaks of Ge-coated nanowires with magnitudes for the structure's total optically driven resistive heating comparable to the magnitude of bare junctions (Figure 3.6d). Extracting precise predictions for the Au temperature

increase in Ge-coated nanowires under laser illumination would require knowledge of both the thermal boundary resistance at the interface between the Ge at the Au, and the thermal conductance of the amorphous Ge.

3.3 Discussion

We have found that the change in polarization response of the photoconductive nanogap antennas with Ge thickness is caused by the tuning of which plasmons dominate at the incident wavelength, the resonant transverse mode or the nonresonant "lightning rod" response. In either limit we have not addressed the precise mechanism of the positive photoconductance of the Ge-coated nanogap structures. There are several potential mechanisms that could contribute to the photocurrent generated in the Ge-coated nanogap structures: direct absorption of light in the Ge located at the gap creating electron-hole pairs via the photovoltaic effect (PVE); driving "hot" carriers generated in the plasmon across the semiconductor-metal barrier, also known as direct electron transfer (DET); or through plasmon-induced resonant energy transfer (PIRET), where the plasmon can directly excite electron-hole pairs in the Ge[2, 45]. Similar studies have also reported photocurrent generation due to the photothermoelectric effect (PTE)[47, 48] and optical rectification[42, 46]. In this study, photocurrent generation only occurs at the nanojunction center, not along the length of the nanowire, and therefore cannot be due to PTE. Additionally, the photocurrent does not trace the signature nonlinear electrical response for optical

rectification, $I_{photo} = \frac{1}{4}\frac{d^2I}{dV^2}V_{ac}^2$. Therefore the photocarriers in Ge-coated bowtie nanojunctions must be generated by a combination of field-enhanced PVE in the Ge and by plasmonic coupling between the Au and the Ge through DET or PIRET. DET has been reported in various plasmon-based photovoltaic devices, but device responsivity is typically inefficient because collection of hot carriers requires careful engineering of geometry and materials to ensure effective coupling between the plasmon, absorption medium, and electrodes[17, 50, 53, 56]. The measured responsivity in the Ge-coated nanogaps in this work calculated to be $\sim 10^{-6}$ A/w at 0.2 V which is comparable to the values listed in Shi, *et al.* (2011)[42], who use electromigrated bowtie nanoantennas on top of graphene, but is significantly lower than the values reported by Tang, *et al.* (2008)[41]. However, their device has a much larger active area and uses crystalline Ge. All three potential mechanisms would have identical polarization dependences; higher fields would produce larger enhancements and more hot carriers, making it difficult to distinguish between these mechanisms based on photoresponse measurements alone. Spectral data or time-resolved measurements could shed light on the relative contribution of each process due to the characteristically short lifetime of hot electrons.

3.4 Conclusion

Bowtie nanowires provide a platform for understanding plasmon response in individual metal-semiconductor-metal nanoantennas. We provide experimental and com-

putational evidence that the dominant plasmon modes in such structures may be controlled by tuning between resonant and nonresonant responses. Photocurrent measurements of Ge-coated nanogap structures dominated by the resonant transverse mode are consistent with measurements of unbroken bowtie nanowires; polarization dependence in both cases follows the known $cos^2(\theta)$ polarization dependence of dipolar optical antennas, with peak photoresponse occurring at an excitation perpendicular to the length of the nanowire ($\theta = 90°$). By optimizing device geometry, this resonant response may be "tuned away" without degrading the Au properties, leaving behind the nonresonant, longitudinal "lightning rod" mode. The nanogap devices operate with a truly nanoscale active region defined by the volume of the interelectrode nanogap. Knowledge of the impact of dielectrics on both resonant and nonresonant local plasmon-enhanced fields is an important step toward fabricating efficient nanoscale light harvesting devices.

Chapter 4

Outlook

This work reviews two projects which make specialized use of the strong field enhancements in bowtie nanowires: Chapter 2 provides a numerical model and experimental evidence for plasmonic optical trapping in these structures and Chapter 3 presents one of a handful of recent studies demonstrating plasmon-assisted photocurrent in individual nanojunctions. The latter builds upon recent work outlining the strength of hybridized, "dark" plasmon modes in bowtie nanoantennas and gives a detailed account of how to manipulate resonant and nonresonant plasmon responses in these structures using the surrounding dielectric environment.

Engineering the plasmon response of nanostructures for use in photosensitive systems has been a highly active area of research for about a decade[53]. The most recent advances in this field have focused on either photocarrier generation in 2D materials, such as graphene[42, 47, 48], MoS_2[43], and InSe[90] as well as hot electron injection in metal-insulator-metal systems[45, 51]. Within the past year, Li, *et al.* (2015)[45], Hong *et al.* (2015)[43], and Lei, *et al.* (2015)[90] have made significant advancements in quantifying the relative contributions of the various plasmon-based photocarrier generation mechanisms present in these geometries, as discussed in Section 3.3. Using this knowledge to effectively integrate plasmon resonant materials into traditional photovoltaic platforms could lead to widespread use of new, and more efficient, meth-

ods for photocarrier generation and collection.

Bibliography

[1] J. B. Herzog, M. W. Knight, Y. Li, K. M. Evans, N. J. Halas, and D. Natelson, "Dark Plasmons in Hot Spot Generation and Polarization in Interelectrode Nanoscale Junctions," *Nano Lett.* **13**, 1359 (2013).

[2] S. K. Cushing, J. Li, F. Meng, T. R. Senty, S. Suri, M. Zhi, M. Li, A. D. Bristow, and N. Wu, "Photocatalytic Activity Enhanced by Plasmonic Resonant Energy Transfer from Metal to Semiconductor," *J. Am. Chem. Soc.* **134**, 15033 (2012).

[3] J. B. Herzog, M. W. Knight, and D. Natelson, "Thermoplasmonics: Quantifying Plasmonic Heating in Single Nanowires," *Nano Lett.* **14**, 499 (2014).

[4] C. Murray, C. Kagan, and M. Bawendi, "Synthesis and Characterization of Monodisperse Nanocrystals and Close-packed Nanocrystal Assemblies," *Annu. Rev. Mater. Sci.* **30**, 545 (2000).

[5] C. F. Bohren, "How can a particle absorb more than the light incident on it?," *Am. J. Phys.* **51**, 323 (1983).

[6] N. Ashcroft and N. Mermin, *Solid State Physics* (Thomson Learning, 1976).

[7] P. Johnson and R. Christy, "Optical Constants of the Noble Metals," *Phys. Rev. B* **6**, 4370 (1972).

[8] D. R. Ward, *Electrical and Optical and Characterization of Molecular Nanojunctions*, PhD thesis Rice University 2010.

[9] D. R. Ward, N. K. Grady, C. S. Levin, N. J. Halas, Y. Wu, P. Nordlander, and D. Natelson, "Electromigrated Nanoscale Gaps for Surface-Enhanced Raman Spectroscopy," *Nano Lett.* **7**, 1396 (2007).

[10] D. R. Ward, N. J. Halas, J. W. Ciszek, J. M. Tour, Y. Wu, P. Nordlander, and D. Natelson, "Simultaneous Measurements of Electronic Conduction and Raman Response in Molecular Junctions," *Nano Lett.* **8**, 919 (2008).

[11] P. Bharadwaj, B. Deutsch, and L. Novotny, "Optical Antennas," *Adv. Opt. Photonics* **1**, 438 (2009).

[12] L. Neumann, J. van 't Oever, and N. F. van Hulst, "A Resonant Scanning Dipole-Antenna Probe for Enhanced Nanoscale Imaging," *Nano Lett.* **13**, 5070 (2013).

[13] W. Zhang, L. Huang, C. Santschi, and O. J. F. Martin, "Trapping and Sensing 10nm Metal Nanoparticles Using Plasmonic Dipole," *Nano Lett.* **10**, 1006 (2010).

[14] Y. Tsuboi, T. Shoji, N. Kitamura, M. Takase, K. Murakoshi, Y. Mizumoto, and H. Ishihara, "Optical Trapping of Quantum Dots Based on Gap-Mode-Excitation of Localized Surface Plasmon," *J. Phys. Chem. Lett.* **1**, 2327 (2010).

[15] M. Righini, G. Volpe, C. Girard, D. Petrov, and R. Quidant, "Surface Plasmon Optical Tweezers: Tunable Optical Manipulation in the Femtonewton Range," *Phys. Rev. Lett.* **100** (2008).

[16] M. Righini, A. S. Zelenina, C. Girard, and R. Quidant, "Parallel and selective trapping in a patterned plasmonic landscape," *Nat. Phys.* **3**, 477 (2007).

[17] A. Sobhani, M. W. Knight, Y. Wang, B. Zheng, N. S. King, L. V. Brown, Z. Fang, P. Nordlander, and N. J. Halas, "Narrowband photodetection in the near-infrared with a plasmon-induced hot electron device," *Nat. Commun.* **4**, 1643 (2013).

[18] M. T. Sheldon, J. van de Groep, A. M. Brown, A. Polman, and H. A. Atwater, "Plasmoelectric potentials in metal nanostructures," *Science* **346**, 828 (2014).

[19] W. Li and J. Valentine, "Metamaterial Perfect Absorber Based Hot Electron Photodetection," *Nano Lett.* **14**, 3510 (2014).

[20] J.-H. Kim and J.-S. Yeo, "Enhanced Detection of Broadband Incoherent Light with Nanoridge Plasmonics," *Nano Lett.* **15**, 2291 (2015).

[21] S. Collin, F. Pardo, F. Bardou, A. Lemaître, S. Averin, and J.-L. Pelouard, "Harvesting light at the nanoscale by GaAs-gold nanowire arrays," *Opt. Express* **19**, 17293 (2011).

[22] K. C. Balram, R. M. Audet, and D. A. B. Miller, "Nanoscale resonant-cavity-enhanced germanium photodetectors with lithographically defined spectral response for improved performance at telecommunications wavelengths," *Opt. Express* **21**, 10228 (2013).

[23] P. Wheeler, *Quantum Shot and Noise Characteristics and in Atomic and Scale*

and Junctions at Liquid and Nitrogen and Room and Temperatures, PhD thesis Rice University 2014.

[24] R. Chen, P. J. Wheeler, and D. Natelson, "Excess noise in STM-style break junctions at room temperature," *Phys. Rev. B* **85** (2012).

[25] D. Natelson, Y. Li, and J. B. Herzog, "Nanogap structures: combining enhanced Raman spectroscopy and electronic transport," *Phys. Chem. Chem. Phys.* **15**, 5262 (2013).

[26] H. Park, A. K. L. Lim, A. P. Alivisatos, J. Park, and P. L. McEuen, "Fabrication of metallic electrodes with nanometer separation by electromigration," *Appl. Phys. Lett.* **75**, 301 (1999).

[27] A. Fursina, S. Lee, R. G. S. Sofin, I. V. Shvets, and D. Natelson, "Nanogaps with very large aspect ratios for electrical measurements," *Appl. Phys. Lett.* **92**, 113102 (2008).

[28] D. R. Ward, G. D. Scott, Z. K. Keane, N. J. Halas, and D. Natelson, "Electronic and optical properties of electromigrated molecular junctions," *J. Phys.: Condens. Matter* **20**, 374118 (2008).

[29] Y. Li, P. Doak, L. Kronik, J. B. Neaton, and D. Natelson, "Voltage tuning of vibrational mode energies in single-molecule junctions," *Proceedings of the National Academy of Sciences* **111**, 1282 (2014).

[30] N. A. Hatab, C.-H. Hsueh, A. L. Gaddis, S. T. Retterer, J.-H. Li, G. Eres, Z. Zhang, and B. Gu, "Free-Standing Optical Gold Bowtie Nanoantenna with Variable Gap Size for Enhanced Raman Spectroscopy," *Nano Lett.* **10**, 4952 (2010).

[31] M. J. Banholzer, J. E. Millstone, L. Qin, and C. A. Mirkin, "Rationally designed nanostructures for surface-enhanced Raman spectroscopy," *Chemical Society Reviews* **37**, 885 (2008).

[32] Z. Ioffe, T. Shamai, A. Ophir, G. Noy, I. Yutsis, K. Kfir, O. Cheshnovsky, and Y. Selzer, "Detection of heating in current-carrying molecular junctions by Raman scattering," *Nat. Nano.* **3**, 727 (2008).

[33] L. Novotny and B. Hecht, *Principles of Nano-Optics* (Cambridge University Press, 2006).

[34] M. W. Knight, *Optoelectronic and Ultraviolet Plasmonics*, PhD thesis Rice University 2014.

[35] M. C. Hegg, M. P. Horning, T. Baehr-Jones, M. Hochberg, and L. Y. Lin, "Nanogap quantum dot photodetectors with high sensitivity and bandwidth," *Appl. Phys. Lett.* **96**, 101118 (2010).

[36] M. Hegg and L. Y. Lin, "Near-field photodetection with high spatial resolution by nanocrystal quantum dots," *Opt. Express* **15**, 17163 (2007).

[37] F. Prins, M. Buscema, J. S. Seldenthuis, S. Etaki, G. Buchs, M. Barkelid, V. Zwiller, Y. Gao, A. J. Houtepen, L. D. A. Siebbeles, and et al., "Fast and Efficient Photodetection in Nanoscale Quantum-Dot Junctions," *Nano Lett.* **12**, 5740 (2012).

[38] M. S. Gudiksen, K. N. Maher, L. Ouyang, and H. Park, "Electroluminescence from a Single-Nanocrystal Transistor," *Nano Lett.* **5**, 2257 (2005).

[39] A. Dorn, H. Huang, and M. G. Bawendi, "Electroluminescence from Nanocrystals in an Electromigrated Gap Composed of Two Different Metals," *Nano Lett.* **8**, 1347 (2008).

[40] S. S. Mousavi, A. Stöhr, and P. Berini, "Plasmonic photodetector with terahertz electrical bandwidth," *Appl. Phys. Lett.* **104**, 143112 (2014).

[41] L. Tang, S. E. Kocabas, S. Latif, A. K. Okyay, D.-S. Ly-Gagnon, K. C. Saraswat, and D. A. B. Miller, "Nanometre-scale germanium photodetector enhanced by a near-infrared dipole antenna," *Nat. Photonics* **2**, 226 (2008).

[42] S.-F. Shi, X. Xu, D. C. Ralph, and P. L. McEuen, "Plasmon Resonance in Individual Nanogap Electrodes Studied Using Graphene Nanoconstrictions as Photodetectors," *Nano Lett.* **11**, 1814 (2011).

[43] T. Hong, B. Chamlagain, S. Hu, S. M. Weiss, Z. Zhou, and Y.-Q. Xu, "Plasmonic Hot Electron Induced Photocurrent Response at MoS2-Metal Junctions," *ACS Nano* **9**, 5357 (2015).

[44] A. L. Falk, F. H. L. Koppens, C. L. Yu, K. Kang, N. de Leon Snapp, A. V. Akimov, M.-H. Jo, M. D. Lukin, and H. Park, "Near-field electrical detection of optical plasmons and single-plasmon sources," *Nat. Phys.* **5**, 475 (2009).

[45] G. Li, C. Cherqui, N. W. Bigelow, G. Duscher, P. J. Straney, J. E. Millstone, D. J. Masiello, and J. P. Camden, "Spatially Mapping Energy Transfer from Single Plasmonic Particles to Semiconductor Substrates via STEM/EELS," *Nano Lett.* **15**, 3465 (2015).

[46] D. R. Ward, F. Hüser, F. Pauly, J. C. Cuevas, and D. Natelson, "Optical rectification and field enhancement in a plasmonic nanogap," *Nat. Nano.* **5**, 732 (2010).

[47] T. J. Echtermeyer, P. S. Nene, M. Trushin, R. V. Gorbachev, A. L. Eiden, S. Milana, Z. Sun, J. Schliemann, E. Lidorikis, K. S. Novoselov, and A. Ferrari, "Photothermoelectric and Photoelectric Contributions to Light Detection in Metal-Graphene-Metal Photodetectors," *Nano Lett.* **14**, 3733 (2014).

[48] N. M. Gabor, J. C. W. Song, Q. Ma, N. L. Nair, T. Taychatanapat, K. Watanabe, T. Taniguchi, L. S. Levitov, and P. Jarillo-Herroro, "Hot Carrier-Assisted Intrinsic Photoresponse in Graphene," *Science* **334**, 648 (2011).

[49] D. Basko, "A Photothermoelectric Effect in Graphene," *Sci* **334**, 610 (2011).

[50] M. L. Brongersma, N. J. Halas, and P. Nordlander, "Plasmon-induced hot carrier science and technology," *Nat. Nano.* **10**, 25 (2015).

[51] C. Clavero, "Plasmon-induced hot-electron generation at nanoparticle/metal-oxide interfaces for photovoltaic and photocatalytic devices," *Nat. Photonics* **8**, 95 (2014).

[52] F. P. García de Arquer, A. Mihi, and G. Konstantatos, "Molecular interfaces for plasmonic hot electron photovoltaics," *Nanoscale* **7**, 2281 (2015).

[53] H. A. Atwater and A. Polman, "Plasmonics for improved photovoltaic devices," *Nat. Mater.* **9**, 205 (2010).

[54] M. W. Knight, H. Sobhani, P. Nordlander, and N. J. Halas, "Photodetection with Active Optical Antennas," *Science* **332**, 702 (2011).

[55] M. W. Knight, Y. Wang, A. S. Urban, A. Sobhani, B. Y. Zheng, P. Nordlander, and N. J. Halas, "Embedding Plasmonic Nanostructure Diodes Enhances Hot Electron Emission," *Nano Lett.* **13**, 1687 (2013).

[56] H. Chalabi, D. Schoen, and M. L. Brongersma, "Hot-Electron Photodetection with a Plasmonic Nanostripe Antenna," *Nano Lett.* **14**, 1374 (2014).

[57] P. Berto, E. B. Urena, P. Bon, R. Quidant, H. Rigneault, and G. Baffou, "Quantitative absorption spectroscopy of nano-objects," *Phys. Rev. B* **86** (2012).

[58] D. R. Ward, D. A. Corley, J. M. Tour, and D. Natelson, "Vibrational and electronic heating in nanoscale junctions," *Nat. Nano.* **6**, 33 (2011).

[59] G. Baffou, R. Quidant, and C. Girard, "Heat generation in plasmonic nanostructures: Influence of morphology," *Appl. Phys. Lett.* **94**, 153109 (2009).

[60] G. Baffou, R. Quidant, and F. J. García de Abajo, "Nanoscale Control of Optical Heating in Complex Plasmonic Systems," *ACS Nano* **4**, 709 (2010).

[61] L. Hirsch, R. Stafford, J. Bankson, S. Sershen, B. Rivera, R. Price, J. Hazle, N. Halas, and J. West, "Nanoshell-mediated near-infrared thermal therapy of tumors under magnetic resonance guidance," *Proceedings of the National Academy of Sciences* (2003).

[62] D. Pissuwan, S. M. Valenzuela, and M. B. Cortie, "Therapeutic possibilities of plasmonically heated gold nanoparticles," *Trends in Biotechnology* **24**, 62 (2006).

[63] R. Huschka, J. Zuloaga, M. W. Knight, L. V. Brown, P. Nordlander, and N. J. Halas, "Light-Induced Release of DNA from Gold Nanoparticles: Nanoshells and Nanorods," *J. Am. Chem. Soc.* **133**, 12247 (2011).

[64] O. Neumann, A. S. Urban, J. Day, S. Lal, P. Nordlander, and N. J. Halas, "Solar Vapor Generation Enabled by Nanoparticles," *ACS Nano* **7**, 42 (2013).

[65] Z. J. Coppens, W. Li, D. G. Walker, and J. G. Valentine, "Probing and Controlling Photothermal Heat Generation in Plasmonic Nanostructures," *Nano Lett.* **13**, 1023 (2013).

[66] A. Cuadrado, J. Alda, F. Javier, and González, "Distributed bolometric effect in

optical antennas and resonant structures," *Journal of Nanophotonics* **6**, 063512 (2012).

[67] G. Baffou, C. Girard, and R. Quidant, "Mapping Heat Origin in Plasmonic Structures," *Phys. Rev. Lett.* **104**, 136805 (2010).

[68] N. J. Hogan, A. S. Urban, C. Ayala-Orozco, A. Pimpinelli, P. Nordlander, and N. J. Halas, "Nanoparticles Heat through Light Localization," *Nano Lett.* **14**, 4640 (2014).

[69] G. Konstantatos, I. Howard, A. Fischer, S. Hoogland, J. Clifford, E. Klem, L. Levina, and E. H. Sargent, "Ultrasensitive solution-cast quantum dot photodetectors," *Nature* **442**, 180 (2006).

[70] J. Tang, K. W. Kemp, S. Hoogland, K. S. Jeong, H. Liu, L. Levina, M. Furukawa, X. Wang, R. Debnath, D. Cha, and et al., "Colloidal-quantum-dot photovoltaics using atomic-ligand passivation," *Nat. Mater.* **10**, 765 (2011).

[71] M. P. van Kouwen, M. H. M. van Weert, M. E. Reimer, N. Akopian, U. Perinetti, R. E. Algra, E. P. A. M. Bakkers, L. P. Kouwenhoven, and V. Zwiller, "Single quantum dot nanowire photodetectors," *Appl. Phys. Lett.* **97**, 113108 (2010).

[72] H. Huang, A. Dorn, V. Bulovic, and M. G. Bawendi, "Electrically driven light emission from single colloidal quantum dots at room temperature," *Appl. Phys. Lett.* **90**, 023110 (2007).

[73] M. H. M. van Weert, N. Akopian, U. Perinetti, M. P. van Kouwen, R. E. Algra, M. A. Verheijen, E. P. A. M. Bakkers, L. P. Kouwenhoven, and V. Zwiller, "Selective Excitation and Detection of Spin States in a Single Nanowire Quantum Dot," *Nano Lett.* **9**, 1989 (2009).

[74] A. Manjavacas, F. J. G. d. Abajo, and P. Nordlander, "Quantum Plexcitonics: Strongly Interacting Plasmons and Excitons," *Nano Lett.* **11**, 2318 (2011).

[75] M. Righini, P. Ghenuche, S. Cherukulappurath, V. Myroshnychenko, F. J. García de Abajo, and R. Quidant, "Nano-optical Trapping of Rayleigh Particles and Escherichia coli Bacteria with Resonant Optical Antennas," *Nano Lett.* **9**, 3387 (2009).

[76] H. Zhang, R. J. Barsotti, C.-L. Wong, X. Xue, X. Liu, F. Stellacci, and J. T. L. Thong, "Polymer-Protected Sub-2-nm-Nanogap Fabrication for Biological Sensing in Near-Physiological Conditions," *Small* **5**, 2797 (2009).

[77] L. Novotny, R. Bian, and X. Xie, "Theory of Nanometric Optical Tweezers," *Phys. Rev. Lett.* **79**, 645 (1997).

[78] P.-Y. Chen, C. Argyropoulos, and A. Alu, "Enhanced nonlinearities using plasmonic nanoantennas," *Nanophotonics* **1** (2012).

[79] L. Huang, S. Maerkl, and O. Martin, "Integration of plasmonic trapping in a microfluidic environment," *Opt. Express* **17**, 6018 (2009).

[80] D. Erickson, X. Serey, Y.-F. Chen, and S. Mandal, "Nanomanipulation using near field photonics," *Lab on a Chip* **11**, 995 (2011).

[81] A. N. Grigorenko, N. W. Roberts, M. R. Dickinson, and Y. Zhang, "Nanometric optical tweezers based on nanostructured substrates," *Nat. Photonics* **2**, 365 (2008).

[82] L. J. Willis, J. A. Fairfield, T. Dadosh, M. D. Fischbein, and M. Drndic, "Controlling Nanogap Quantum Dot Photoconductivity through Optoelectronic Trap Manipulation," *Nano Lett.* **9**, 4191 (2009).

[83] V. Garcés-Chávez, R. Quidant, P. J. Reece, G. Badenes, L. Torner, and K. Dholakia, "Extended organization of colloidal microparticles by surface plasmon polariton excitation," *Phys. Rev. B* **73** (2006).

[84] T. S. Mentzel, D. D. Wanger, N. Ray, B. J. Walker, D. Strasfeld, M. G. Bawendi, and M. A. Kastner, "Nanopatterned Electrically Conductive Films of Semiconductor Nanocrystals," *Nano Lett.* **12**, 4404 (2012).

[85] K. M. Evans, P. Zolotavin, and D. Natelson, "Plasmon-assisted photoresponse in Ge-coated bowtie nanojunctions," *ACS Photonics* **in press** (2015).

[86] T. Donovan, W. Spicer, J. Bennet, and E. Ashley, "Optical Properties of Amorphous Germanium Films," *Phys. Rev. B* **2**, 397 (1970).

[87] S. Tomlin, E. Khawaja, and G. Thutupalli, "The optical properties of amorphous

and crystalline germanium," *J. Phys. C: Sol. State Phys.* **9**, 4335 (1976).

[88] M. W. Knight, Y. Wu, J. B. Lassiter, P. Nordlander, and N. J. Halas, "Substrates Matter: Influence of an Adjacent Dielectric on an Individual Plasmonic Nanoparticle," *Nano Lett.* **9**, 2188 (2009).

[89] N. Liu, M. L. Tang, M. Hentschel, H. Giessen, and A. P. Alivisatos, "Nanoantenna-enhanced gas sensing in a single tailored nanofocus," *Nat. Mater.* **10**, 631 (2011).

[90] S. Lei, F. Wen, L. Ge, S. Najmaei, A. George, Y. Gong, W. Gao, Z. Jin, B. Li, J. Lou, and et al., "An Atomically Layered InSe Avalanche Photodetector," *Nano Lett.* **15**, 3048 (2015).